Appl. Phys. A 34, 73–94 (1984)

Applied Physics A Solids and Surfaces

Sputtering Studies with the Monte Carlo Program TRIM.SP

J. P. Biersack* and W. Eckstein

Max-Planck-Institut für Plasmaphysik, Euratom-Association,
D-8046 Garching bei München, Fed. Rep. Germany

Received 11 April 1983/Accepted 5 January 1984

Abstract. The Monte Carlo Program TRIM.SP (sputtering version of TRIM) was used to determine sputtering yields and energy and angular distributions of sputtered particles in physical (collisional) sputtering processes. The output is set up to distinguish between the contributions of primary and secondary knock-on atoms as caused by in- and outgoing incident ions, in order to get a better understanding of the sputtering mechanisms and to check on previous theoretical models. The influence of the interatomic potential and the inelastic energy loss model as well as the surface binding energy on the sputtering yield is investigated. Further results are sputtering yields versus incident energy and angle as well as total angular distributions of sputtered particles and energy distributions in specific solid angles for non-normal incidence. The calculated data are compared with experimental results as far as possible. From this comparison it turns out that the TRIM.SP is able to reproduce experimental results even in very special details of angular and energy distributions.

PACS: 79, 20

Sputtering of target atoms from solid surfaces under ion bombardment has long been studied for both the physical understanding of the collisional processes involved, and for various practical reasons as well, e.g. sputter surface cleaning or sputter thin film deposition in large scale technical applications, or as a potent research tool for high-resolution depth profiling SIMS [1], or last but not least in plasma-wall interaction problems (erosion of first wall materials and plasma contamination) in fusion devices [2]. The amount of experimental data has been growing at a steady rate over the past 20 years (see, for example, the last exhaustive compilation by Andersen and Bay [Ref. 3, Chap. 4]), and numerous publications have appeared since then, on theoretically predicting sputtering yields (see the references in the recent review articles by Sigmund [Ref. 3, Chap. 2], Robinson [Ref. 3, Chap. 3], Jackson [4] and Harrison [5].

Analytical studies based on transport theory [Ref. 3, Chap. 2] introduce special simplifying assumptions in order to be analytically tractable, e.g. the use of power potential approximations [6–8] to the real interatomic potential. In analytical theories it is also difficult to include all collisional processes leading to sputtering, for example, the sputtering theory of Sigmund [8] considers the cascades caused by the incident ion, while the recent theory of Littmark [9] concentrates on the emission of primary recoils by the backscattered fraction of ions. The last example also indicates that the fate of the ions has to be pretty well known for reliable predictions of sputtering yields, which brings about another problem: If the angle of ion incidence is not normal, but rather glancing with respect to the surface, the proximity of the ion trajectory to the surface may enhance the sputtering, but – on the other hand – also may lead to increased ion losses through the free surface and result in a decrease of sputtering. The delicate balance of these counteracting effects

* Visitor from Hahn-Meitner Institut, Berlin

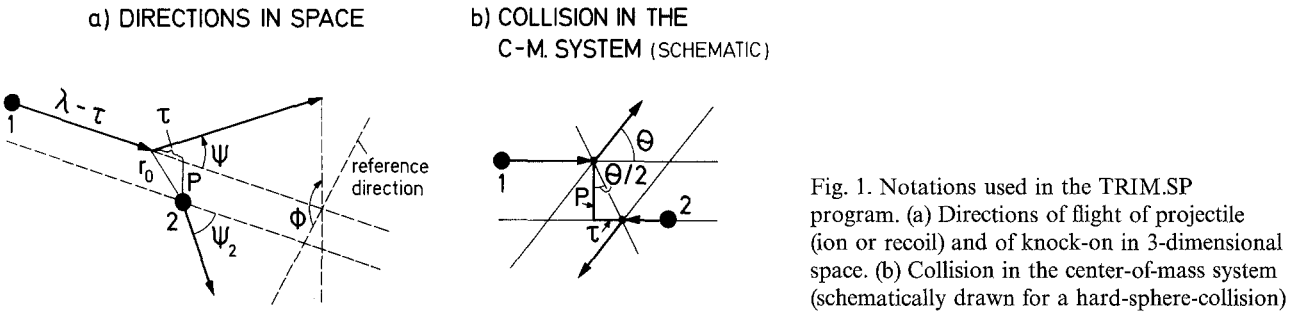

Fig. 1. Notations used in the TRIM.SP program. (a) Directions of flight of projectile (ion or recoil) and of knock-on in 3-dimensional space. (b) Collision in the center-of-mass system (schematically drawn for a hard-sphere-collision)

creates problems in any present analytic theory. In view of these difficulties, a straightforward computer simulation of the collisional processes near a free surface appeared worthwhile, not only for studying the various mechanisms and testing the existing theories, but – even more important – for providing realistic predictions in practical cases, such as e.g. in fusion research (plasma-wall interaction, neutral beam injection), where it is virtually impossible to provide all necessary data for a complex machine by individual measurements.

For this purpose, the previously existing TRIM program [10] was modified in order to follow the recoil atoms as well as the ion. The TRIM version TRIM.SP turned out to be sufficiently computer efficient, so that – in connection with modern high speed computers – enough ion histories could be processed for obtaining statistically meaningful results. It turned out that this program could be applied in fusion research, where extremely low sputtering yields are encountered, e.g. $\lesssim 0.1$ for low energy plasma particles H, D, T, He [11–20]. The program will be described in the following chapters, together with some results, which have been selected either to check on previously predicted basic properties and dependences, or to illustrate interesting new features, e.g. on angular or energy distributions which were previously not clearly recognized.

1. The TRIM Sputtering Program

1.1. Basic Principles

The TRIM program for the *tr*ansport of *i*ons in *m*atter was developed with the main goal of providing a program which is particularly computer efficient and still maintains a high degree of accuracy. The details of the program have already been described in [10], so that we can limit the present description to the basic principles and to the newly introduced extensions which were necessary to follow all particles in 3-dimensional space, to treat mixed recoil cascades, and finally to simulate different surfaces, i.e. an "ideally smooth" surface which assumes all surface atoms to be in a plane, and a "random" surface, where the amorphous material reaches up to the surface. As described in [10], the TRIM program is based on the assumption of an amorphous target material. For targets with randomly oriented crystallites we assume that this is a sufficient approximation, since directional effects will be assumed to be mostly compensated.

Basically, the incident ions and the recoil atoms are followed throughout their slowing-down process until their energy falls below a predetermined energy; usually 5 eV is used for the incident ion, and the surface binding energy is used for the knock-on atoms. In order to speed up the computation, a check was built in to determine whether a recoil atom has moved so far from the surface or has lost so much energy that it is unable to reach the surface; if that is the case, it is not followed any further as a candidate for sputtering.

The program is arranged to follow the knock-on atom created by the incident ion. This primary knock-on atom (PKA) gets the label $i=1$. In a further collision this PKA is labeled $i+1$, whereas the information of the newly created knock-on atom (SKA) is stored under label i. If the PKA is sputtered or disregarded for reasons mentioned in the last paragraph, the program returns to the last recoil atom with label i. Now this SKA is followed in the same way as the PKA. Finally, the label is counted down to $i=0$, which is the ion itself. Then the ion is moved to the next collision and the procedure starts again. The complete data set of one recoil contains the following information: An atom, created by an inward or outward moving ion, primary or secondary knock-on, depth of origin, present energy, present position, and present direction of motion (the last two in 3-dimensional space).

Another procedure, which ensures the most efficient use of computer memory as the number of data sets stored equals just the generation number in a collision cascade, is to always follow the newly created knock-on atom, say with label $i+1$, and store the information of the last particle with label i ($i=0$ would be the ion itself). If that atom leaves the surface as a sputtered particle or is disregarded for the reasons

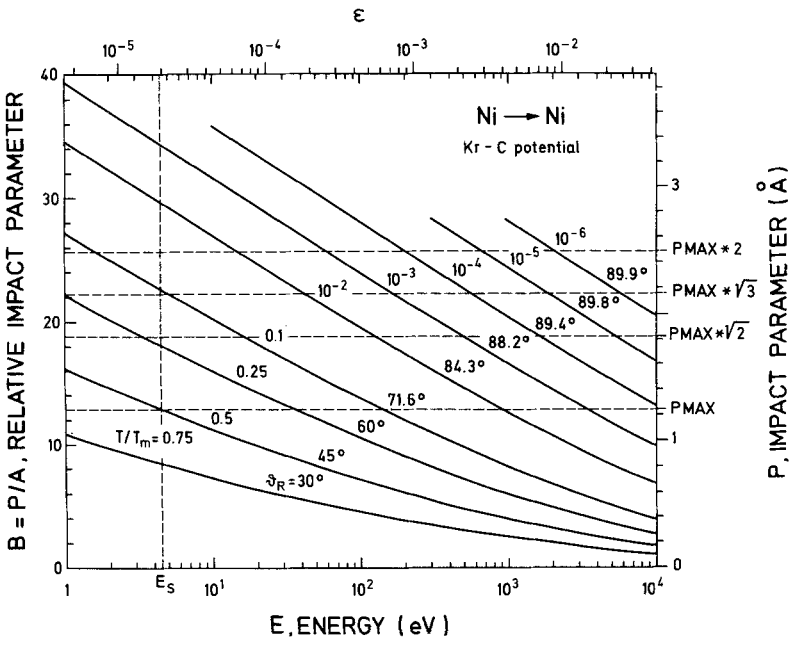

Fig. 2. Curves of constant relative elastic energy transfer T/T_m in a collision versus the impact parameter P (or the relative impact parameter B, A is the Firsov screening length) and the impact energy E for Ni–Ni collisions. T_m is the maximum transferable energy. The Kr–C potential was used as the interaction potential. Maximum impact parameters P_n (Sect. 2.2) and the surface binding energy E_S (Sect. 2.3), are indicated. ϑ_R is the recoil angle in the laboratory system

mentioned above, the program returns to the previous atom with label i. If, however, a new recoil was created, now with label $i+1$, this will be treated first (in the same manner as described before for i).
Spike effects [Ref. 3, Chap. 2] are not taken into account in this treatment.

1.2. Transport of Ions and Recoils

The motion of the incident ion and of the recoiling atoms is treated in the same way: Any particle moves along a mean free path $\lambda = N^{-1/3}$ (N is the atomic density in the target) before it encounters the next collision partner with an impact parameter P between 0 and $P_{max} = \pi^{-1/2} N^{-1/3}$. This procedure ensures that the proper atomic density is maintained, i.e. 1 target atom in a volume $\lambda \cdot \pi P_{max}^2 = N^{-1}$. The impact parameter P and the azimuth angle Φ are determined by random numbers. From the projectiles position and direction and the quantities P and Φ, the position of the target atom is determined (Fig. 1). The collision will only occur if the target-atom position is determined to be within the boundaries of the solid (Fig. 3). The collision is simulated in the TRIM program by the subroutine MAGIC, which determines the scattering angle θ and the transferred energy T with an average precision of about 1%. From this, the new flight directions and energies of the incident particle and knock-on atom are determined. As the subroutine MAGIC also yields the distance of closest approach r_0, the electronic energy loss can be determined as a function of r_0 in the model of Oen and Robinson [21]. In constructing the trajectory of the incident particle, one has to note that the point of deflection is shifted back in the laboratory system by an amount τ, the so-called "time integral". This shift becomes significant at low energies [22], and can be easily calculated in this case by the hard sphere approximation, i.e. $\tau = P \cdot \tan\theta/2$, where θ is the scattering angle in the center-of-mass system (Fig. 1b).
At low energies the maximum impact parameter P_{max}, as described above, is too small to account for all elastic collisions. This is demonstrated in Fig. 2, where it can be seen that at energies near the surface binding energy, E_S (Sect. 1.3), about half the maximum transferable energy can be given to another atom at impact parameters larger than P_{max} [23]. For this reason additional simultaneous scattering events are taken into account. Atoms are randomly chosen in ring cylinders of equal volumes defined by

$$\lambda\pi(P_{n+1}^2 - P_n^2) = N^{-1}, \quad n = 1, 2, \ldots$$

$$P_n = P_{max} \cdot \sqrt{n}$$

maintaining the proper density in the ring cylinders ($n > 1$). The elastic energy loss and the changes in the scattering angle due to the additional scattering processes are taken into account. The number of additional ring cylinders ($n > 1$), which have to be applied, has to be checked individually. Recoil atoms created in the cylinder rings ($n > 1$) are not followed. (This approximation is justified because it changes the sputtering yield by less than a few percent for all cases investigated). In an earlier version of TRIM.SP, TRSPCR1, which was used for most calculations before this paper, only $n = 1$ was used.
To reduce computer time the program calculates the range of a recoil atom ($Z_1 \approx Z_2$) in the solid. An upper

limit R of the recoil range is approximated by $R=(\varepsilon^{0.3}+0.1)^3/Na^2$ with the atomic density N, the screening length a and the reduced energy ε. ε is defined by $\varepsilon=a M_2 E/Z_1 Z_2 e^2(M_1+M_2)$, where E is the energy, Z and M the charge and the mass of the colliding particles, respectively. The formula was derived by comparison with experimental and calculated range data. If a target atom is set in motion at a depth x larger than its range R, the target atom is not followed further. This cutoff value R was used in all earlier calculations with TRIM.SP. But it was found (see also [7]) that the range of the cascade can be larger by a factor of 2 than the range of the originally started target atom, increasing the sputtering yield by as much as 50%. We have therefore increased the cutoff range R by at least a factor $f=2$ in all calculations for this paper. Computer time needed is roughly proportional to f.

The TRIM program assumes the validity of the binary encounter model, i.e. the projectiles (incident ion or recoil atoms) encounter target atoms sequentially, one by one. This same assumption is also implicitly inherent in all analytic theories which are based on linearized Boltzmann equations. Even the simple definitions of nuclear energy loss and straggling rely on this assumption. Nevertheless, in the community of Monte-Carlo users, this assumption seems always to be a matter of some concerns (see also [Ref. 3, Chap. 3]). Our confidence in the binary encounter model rests mainly upon two arguments:

(i) At high energies, where the effective potentials are rather soft (behaving, for example, like $r^{-1\cdots-3}$), all significant collisions happen with impact parameters which are small compared to the separations of the target atoms.

(ii) At low energies, the potentials become so hard (e.g. like a $r^{-5\cdots-7}$ potential), that the close collisions actually could be well described by hard-sphere-collisions, occuring at the exactly calculated radius of closest approach $r_0(E,P)$. Simultaneous collisions with more distant atoms become important and cannot be neglected. Here again, the ion trajectory appears as a sequence of binary collisions separated by very short distances.

1.3. Binding Energies

The surface binding energy E_S has a significant influence upon the total sputtering yields, and also upon the energy and angular distributions of the low energy sputtered atoms. As an input for E_S, we have generally used the heat of sublimation H_S [24, 25] which amounts to about 4 eV for fcc metals such as Cu, Ni, and Au and about 7 eV for bcc metals such as Nb and Mo (the most extreme values are 0.8 eV for Cs, and 8.7 eV for W) [26]. The surface binding energy acts in the form of a planar attractive potential upon the atoms which attempt to leave the surface, and cause a refraction or even a reflection back into the solid, depending upon energy and angle of the moving atom. As a different choice for the surface binding a scalar potential [8] can also be applied.

The program provides for subtracting a binding energy E_B, whenever a new recoil is created. Since, for each new recoil, a vacancy will be left behind, E_B might be set equal to the vacancy formation energy, E_{1V}^F, i. e. about 1 eV for fcc metals and about 3 eV for bcc metals. However, binding energies of this magnitude are of little influence on the sputtering results, since E_B is usually small compared to the transferred energy T at high energy bombardment. In addition, at all energies most sputtered atoms originate in the surface layer – not in the bulk – where the subtraction of E_{1V}^F is not applicable.

Another model [27] states that the bulk binding energy E_B should be of the same magnitude as the surface binding energy E_S for all atoms in the solid deeper than the surface layer. Still another model used in computer simulation [Ref. 3, Chap. 3] uses the relation that the sum of bulk and surface binding energy is equal to the heat of sublimation H_S. This relation is used in MARLOWE, where a nonzero value, $E_B \simeq 0.2$ eV, is applied only to account for realistic lengths of collision sequences [28]. A close comparison of MARLOWE results with results from classical dynamical calculations determined the choice of E_B. This is consistent with $E_B=0$ eV for a randomized target as used in TRIM.SP – All three models can be applied in TRIM.SP.

1.4. Potentials and Nuclear Stopping

In TRIM.SP the Molière potential [29] or the Kr-C potential [30] can be used. The Kr-C potential with the Firsov screening length [31] describes the interaction especially at low ε-values more realistically than the Molière potential. The Kr-C potential was not only found to be a good average of a large series of individually calculated potentials [30] but it is also supported by low energy precision experiments, e.g. recent range measurements [32] or scattering experiments [33] which can be well interpreted by using the Kr-C potential [34].

At the much higher ε-values of the incident light ions considered here (mainly H^+, D^+, He^+), the differences between Molière and Kr-C potentials vanish; besides, if H^+ and D^+ are considered to move as mere point charges through the solid, not carrying electrons along, they would probe only the electro-static potential inside the target atoms which is sufficiently well described by the Molière function. For low energy

heavy ions, e.g. Ar^+, Kr^+, impinging on medium heavy targets, however, the corresponding ε-values are rather small and the use of the proper potential becomes essential. For example, at $\varepsilon = 10^{-2}$ nuclear stopping power becomes about 30% lower for realistic potentials than for the Molière potential, and yields accordingly lower sputtering yields (Sect. 2.1).

1.5. Inelastic Energy Losses

The electronic energy loss ΔE_e can be chosen in the TRIM.SP program from three options: 1) steady slowing-down using either an E^p, $p \simeq 1/2$, stopping power (for $\varepsilon < 20$), or using the well known interpolation scheme between the above Lindhard-Scharff and the Bethe-Bloch stopping powers [35–37] which is valid up to relativistic energies. For the hydrogen and helium isotopes H, D, T, ^{3}He, ^{4}He which are frequently considered here as projectiles, the stopping power parameters of [37] are used as input into this interpolation scheme. For other, heavier ions, the Lindhard and Scharff [38] $k\sqrt{E}$ is used for the low energy part (with an appropriate correction factor, if known from experiments), and for the high energy part, the Bethe-Bloch formula is applied with the Sternheimer mean ionization energy, as given in [10].

In the second possible choice 2), an individual energy loss, $\Delta E_e(r_0)$ [21], which depends on the interpenetration of shells (r_0 being the distance of closest approach in the collision), and which introduces an electronic energy loss straggling of about the same magnitude as predicted by Lindhard and Scharff [38], is subtracted at each collision. The quantity $\Delta E(r_0)$ contains the same parameters k and p as used in the steady slowing down.

The third possibility 3) consists of mixing the previous steady (nonlocal) and collision-dependent (local) electronic stoppings, e.g. in a 50% – 50% modus. It should be noted that for low energies, good theoretical understanding is still lacking, and experimental data on electronic stopping are scarce and difficult to obtain for low velocity projectiles.

1.6. Treatment of the Surface

The TRIM program has been developed for randomized targets [10] thus avoiding the lengthy procedure for determining the position of the next collision partner which is necessary for a crystal structure. Instead, subsequent collisions are assumed to happen after travelling a given mean free flight path λ with the target atom in a random lateral position within a "disk" of radius P_{max} (Fig. 3). In order to account for the surface, the targetatom position is checked as to whether it is in the bulk, i.e. deeper than $2P_{max}$ (there is no target atom

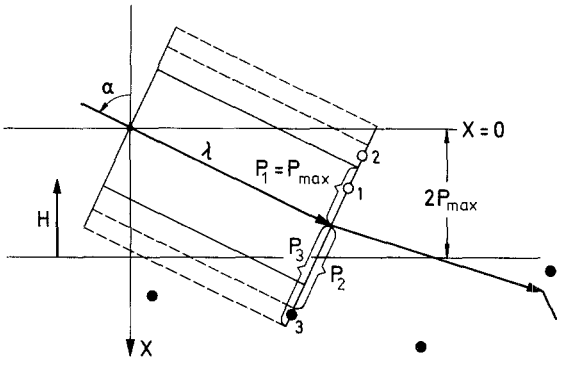

Fig. 3. Surface treatment in the TRIM.SP program ("atomically rough" surfaces): Target atoms (●) exist only at depths $x > 2P_{max}$. If the target atom's position is found at depth $x < 2P_{max}$ this target atom will be disregarded (open circles denoted by "1" or "2"). In the figure a target atom is only found for $n = 3$. Note that after the first collision the trajectory is out of plane. Also target atoms are located outside the plane. H is the height above the target atoms, in which a nonlocal inelastic energy loss can be applied

between $x = 0$ and $x = 2P_{max}$). If that condition is not fullfilled, i.e. $x_{Target} < 2P_{max}$ (Fig. 3), additional tries are made in ring cylinders, as described in Sect. 1.2. If there is again no target atom found at a depth $x > 2P_{max}$, then the projectile moves on straight ahead. The notation "projectile" is used here for the ion or any recoil atom moving in the solid. For the examples of this paper, shown in Sect. 2, we have exclusively used this surface model, which we consider to be more realistic than a planar surface.

In the earlier TRIM.SP version, TRSPCR1, a different surface treatment was applied. The region in which no target atom can be found is P_{max} instead of $2P_{max}$. If the first attempt to find a target atom fails, only a second try finding a target atom between P_{max} and $2P_{max}$ is made. This model underestimates the scattering at the surface resulting in minor deviations in the angular [39] and energy [40] distributions. This treatment was used in [18–20, 39, 40].

Still another possible surface treatment of the TRIM.SP program is indicated: The uppermost layer of the target atoms (or of some adsorbed other atoms) is assumed to form a perfect plane at $x = P_{max}$ with random locations in y and z. In this case of an "atomically smooth" surface, a projectile which has moved into the surface region (from the inside or outside), will find its collision partner only in the intersection of this atomic plane and the "target disk". This requires just one random number for the lateral displacement of the target atom between $-P_{max}$ and $+P_{max}$. For applying the program, for example, to an adsorbed surface layer, it is easy to assign specific values Z_a, M_a to these surface atoms, different from the

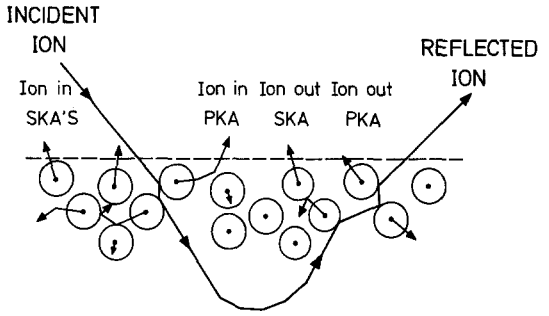

Fig. 4. The four possible sputtering events which are distinguished in the TRIM output. From left to right: (1) Secondary knock-ons (SKA) and (2) primary knock-on (PKA) caused by the incident ion, and (3) SKA and (4) PKA from the backscattered ion. All four contributions have their significance depending on angle, energy and mass of the incident ion

target atoms in the bulk. This surface model has often been applied in previous publications [11–17].

If a recoil has moved into a position $x<0$, it is considered a candidate for sputtering. After reducing its energy component normal to the surface by the action of the planar surface potential which represents the surface binding energy, it will either be reflected back into the solid (and followed through further collisions), or it will leave the surface with the reduced energy and refracted emission angle as a sputtered particle.

2. Results and Discussion

The TRIM.SP program was applied to a series of cases which were selected for the purpose of illustrating the typical features of sputtering. Most emphasis is laid, however, on light ion sputtering, not only because of its relevance to fusion devices, but also for its more interesting variety of processes. While heavy ions of multi-keV energies were found to sputter mainly through collision cascades caused by the incident ion, the light ions were seen to sputter via primary and secondary knock-ons of the backscattered ions [41], as well as of the incident ions, their relative contributions changing drastically with energy and angle of incidence. The importance of the various processes was not intensively investigated previously [42], and the low energy light ion sputtering was studied by an appropriate analytical theory only in a few cases [9, 43].

In the present paper we performed studies using the TRIM.SP program with the following output:

(*i*) total sputtering yields, subdivided into sputtering by incident and reflected ions, primary and secondary knock-ons (Fig. 4)

(*ii*) ion reflection (backscattering),

(*iii*) sputtered particle distributions in energy, in depth of origin,

(*iv*) two-dimensional distributions in polar and azimuthal angles, and angle-energy correlations.

The cases which will be presented in this paper, range from light ions, H^+, D^+, He^+ to heavy ones, Ne^+, Ar^+, Xe^+, impinging on carbon, nickel, and molybdenum within the energy range from 30 eV to 200 keV. The results will be discussed with respect to other theories, and will be compared with experimental data. We will also comment on the influence of different potentials, inelastic energy loss models and binding energies on the sputtering yield, and find out about the relative importance of the different processes of sputtering (Fig. 4). Finally, some special features in the angular and energy distributions of sputtered particles will be predicted.

2.1. The Choice of Input Parameters

As an example we will discuss the sputtering yield of Ni by Ne bombardment.

The influence of the chosen interaction potential (ion-atom and atom-atom potentials) on the sputtering yield Y is shown in Fig. 5a. The Molière potential (with Firsov screening length) gives sputtering yields which are about 30% higher than values calculated with the Kr-C potential (with Firsov screening length). Yields calculated with the Molière potential but with a reduced screening length [28] (80% of Firsov screening length) are very close to those calculated using the Kr-C potential. The Kr-C potential is applied for all following results in this paper.

The two inelastic energy loss models, the nonlocal LS model and the local OR formula, give sputtering yields which are about 15% different as long as no inelastic nonlocal energy loss outside the target atoms (in the region $x<2P_{max}$) is taken into account (Fig. 5b). An additional nonlocal inelastic energy loss in the region $x<2P_{max}$ for a distance $H=d/2$ (d: lattice distance) due to the electron selvage at the surface decreases the sputtering yield about 25% and will change somewhat the angular distribution for grazing exit angles. It is easily demonstrated analytically that this additional inelastic nonlocal energy loss outside the target acts as an increase in the actual surface binding energy [44]. The nonlocal inelastic energy loss [38] was derived only for the bulk. Therefore we applied nonlocal inelastic energy loss only inside the target ($x>2P_{max}$, $H=0$), whereas a local inelastic energy loss is taken into account whenever a collision occurs. For all the following data we used a 50% to 50% modus of local and nonlocal losses for the heavy particles and the data of [37] for the inelastic losses of

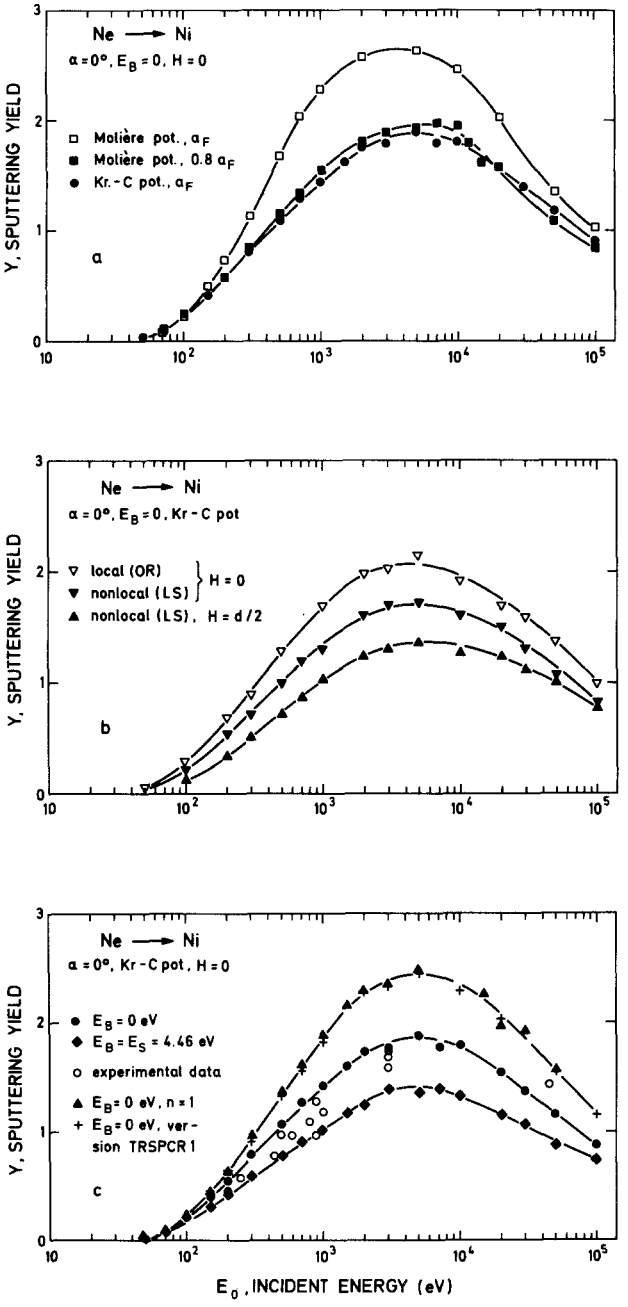

Fig. 5a–c. Sputtering yield Y versus the incident energy E_0 for the bombardment of Ni with Ne at normal incidence, $\alpha=0°$: (a) Dependence of the yield on the interaction potential: □ Molière potential (Firsov screening length, a_F). ■ Molière potential (80% of Firsov screening length). ● Kr–C potential (Firsov screening length). (b) Dependence of the yield on the inelastic energy loss: (I) No nonlocal loss for $x<2P_{max}$ ($H=0$). ▽ Local loss (Oen-Robinson formula). ▼ Nonlocal loss (Lindhard-Scharff model). (II) Nonlocal loss outside the target for ▲ $x>d/2$ ($H=1.76$ Å), where d is the Ni lattice constant. (c) Dependence of the yield on the binding energies: ● Bulk binding energy, $E_B=0$ eV. ◆ Bulk binding energy E_B equal to the surface binding energy E_S for layers deeper than the surface layer. ○ Experimental data. ▲ $E_B=0$, use of inner cylinder only ($n=1$, Sect. 2.2). + $E_B=0$, calculated data with the earlier TRIM.SP version, TRSPCR1. Lines drawn to guide the eye

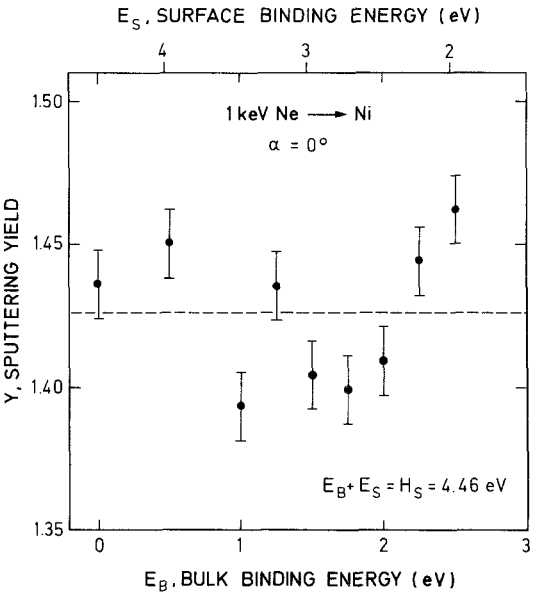

Fig. 6. Sputtering yield Y versus the bulk binding energy E_B for 1 keV Ne bombardment of Ni at normal incidence. The surface binding energy E_S is also varied according to the formula $E_B+E_S=H_S=4.46$ eV, where H_S is the heat of sublimation. The error bars give a statistical error of 1σ (66% confidence)

H and He. In the earlier TRIM.SP version TRSPCR1 an inelastic energy loss in the surface region ($0\leqq x\leqq P_{max}$) was always taken into account.

The dependence of the sputtering yield on different binding energies is shown in Fig. 5c. The model applying a bulk binding energy $E_B=E_S$ for recoil atoms generated at deeper layers ($x>2P_{max}+\lambda$) results in sputtering yields about 25% lower than the model taking $E_B=0$ eV. The latter model is a special case of the model, where $E_B+E_S=H_S$ (H_S; heat of sublimation). Changing E_B and E_S according to this relation does not alter the sputtering yield as demonstrated in Fig. 6. Experimental results do not give a limit for a preference of any of the different models, see Fig. 5c. We decided to use the model with $E_B=0$ eV for the calculations of the following results. The reasons for that decision are:

1) Comparisons of results calculated with the Monte Carlo program MARLOWE with results from dynamical calculations give no hint for a bulk binding energy ([44] and [Ref. 3, Chap. 3]) (except for linear collision sequences [28]),

2) it is not known, what the actual value for E_B in a randomised target and for different materials should be,

3) the use of a bulk binding energy, $E_B\neq 0$ eV, does not change the sputtering yield, if $E_B+E_S=H_S$ is fullfilled,

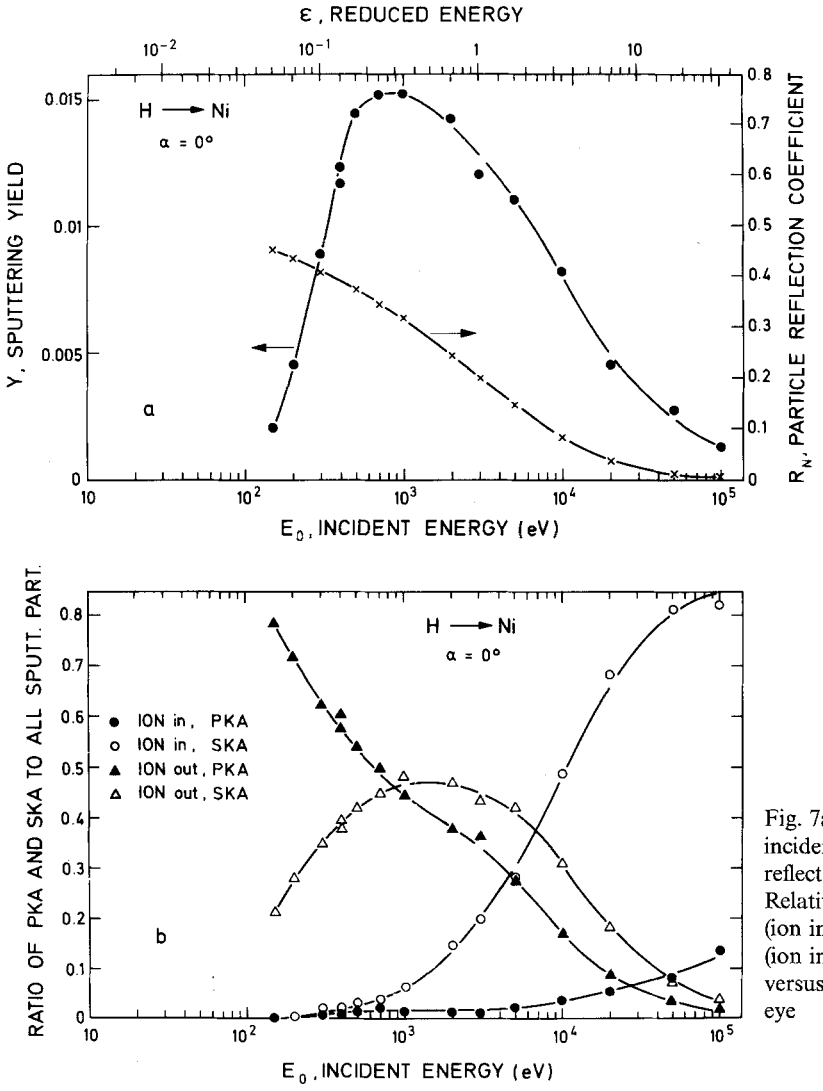

Fig. 7a and b. H bombardment of Ni at normal incidence, $\alpha = 0°$. (a) Sputtering yield Y and particle reflection coefficient R_N versus incident energy E_0. (b) Relative contribution of primary knock-ons, PKA (ion in and ion out), and secondary knock-ons, SKA (ion in and ion out), to the total sputtering yield Y versus incident energy E_0. Lines drawn to guide the eye

4) the results in Fig. 5c show only a difference of about 25% in the yield and nearly no change in the energy and angular distributions (shown later in the paper),
5) from the results in Fig. 5 one cannot expect that the absolute accuracy is better than about 30% which include the results of all models.
In Fig. 5c it is also demonstrated that, taking no additional ring cylinders (only $n = 1$) into account, the yield data coincide with the data gained with the older TRIM.SP version, TRSPCR1, which are about 30% higher than the new data. For the light ions this difference between old and new yield results is smaller, less than 5% for H bombardment of Ni.

2.2. *Contribution of Various Mechanisms*

The first investigation is concerned with total sputtering yields as a function of energy, and the analysis of mechanisms in terms of primary or secondary knock-on atoms, caused by incident or backscattered ions, as indicated in Fig. 4. In [42, 15] 8 instead of 4 different mechanisms have been mentioned. However, we find it difficult to distinguish between atoms sputtered from the surface or the bulk when assuming an amorphous solid, particularly since every ejected atom will undergo additional collisions upon leaving the material.
As target material, nickel is considered with a surface binding energy (= heat of sublimation) of 4.46 eV, and the bulk binding energy assumed to be zero. The first results are shown for light ions, H^+, $^4He^+$ at normal incidence. The upper parts (a) of Figs. 7 and 8 show the total sputtering yields and, for comparison, the particle reflection. This should be compared to the lower parts (b), where the sputtering yield is split up into the four mentioned processes. As well known [45], for all light ions ^1H...^4He at energies below 100 eV, the reflection rises to above 40% and the sputtering is mainly due to

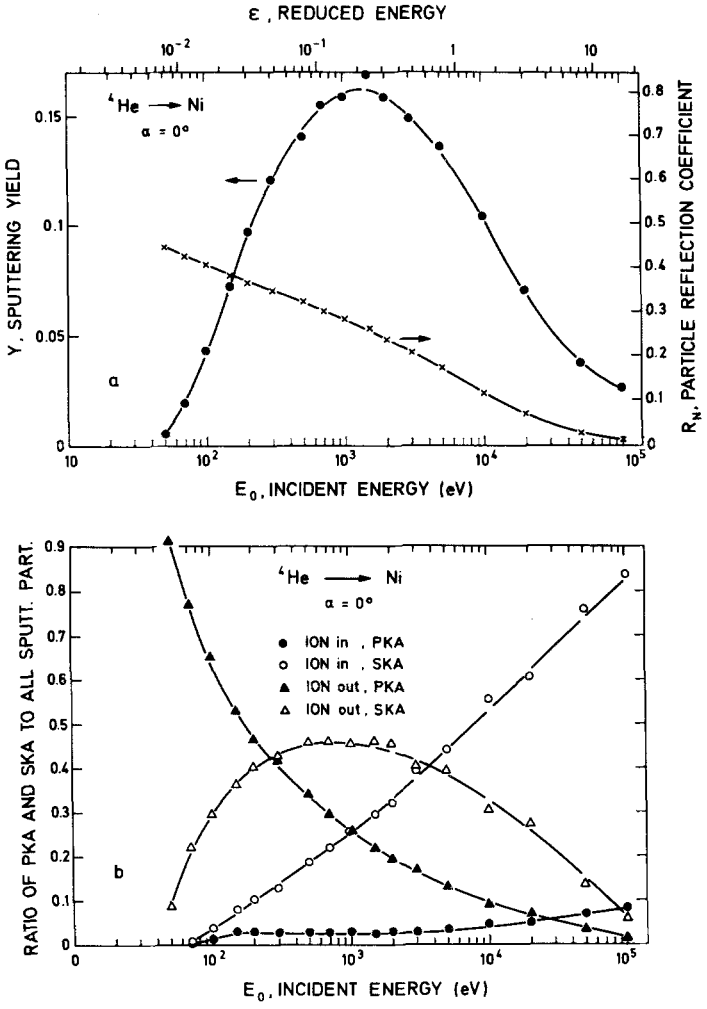

Fig. 8a and b. ^{4}He bombardment of Ni at normal incidence, $\alpha = 0°$. Description the same as for Fig. 7

primary knock-on atoms (PKA) created by reflected ions. This is a special case which has been discussed by Behrisch et al. [42], and has been treated by Littmark and Fedder in an analytical theory [9].

At slightly higher energies, between 0.2 and 5 keV for the considered light ions, secondary knock-on atoms (SKA) of both reflected and incident ions are seen to contribute significantly, and above 5 keV the SKA's of the incident ions alone become dominant. This is the energy regime, where the collision cascade theory [8] should be applicable, if a surface correction is not important.

For heavier incident ions, Ne^+, Ar^+, Xe^+, the contributions of PKA's and SKA's of reflected ions naturally diminish, and the SKA's of the incident ions dominate the sputtering, as illustrated in Figs. 9–12. For Xe^+ on nickel similar features are observed in Fig. 12a and b, except that due to the heavier ion mass no backscattering of Xe occurs from Ni. This leaves only the contribution of SKA's (≅90%) and PKA's (≅10%) from the incident ions over the entire energy range from 70 eV to 100 keV. The break-up into relative fractions of the individual contributions (in part b of the figures) is not very sensitive to the choice of the potential.

In Fig. 9c the relative fractions of sputtered energy carried with the sputtered particles due to the four processes are shown. The contribution of PKA to the sputtered energy is larger than 35% over the whole energy range investigated. A comparison with Fig. 9b tells that the mean energy of PKA is larger than the mean energy of SKA. This is demonstrated in Fig. 10. The PKA created by an ion out have the highest mean energy (they are the elephants between the mice [27]). The mean energy of all sputtered particles show a weak dependence on the incident energy.

With the presently studied heavy ions, e.g. Ar^+, at 1...100 keV incident energy, we are in the domain of applicability of the Sigmund theory [8]. For the potentials used in the TRIM program, the corresponding nuclear stopping powers $S_n(E)$, are also precisely known [30]. It is therefore possible to compare a rigorous treatment of collision cascades with the analytical treatment in transport theory approximations (e.g. in the differential cross-sections, neglect of τ etc.) and simplifying assumptions (neglect of the free surface in ion motion etc.). In the comparison we have applied Sigmund's formalism [8], with a damage energy at the surface $F_D(E, x=0) = \alpha \cdot S_n(E)$. We use $\alpha = 0.3$ and $S_n(E)$ as given analytically in [30] for Molière and Kr-C potentials. The results are depicted as thin solid lines in Fig. 11a. Some deviations occur, particularly at the low and high energy ends of the curves. One has to say that the analytical formula of Sigmund [8] is not applicable for energies below 500 eV. On the high energy end of the curve the analytical curve overshoots the TRIM results, connected with a shift of the maximum towards higher energies.

Figures 13–15 show the yield and the contributions of the four processes versus the angle of incidence, in respect to the surface normal. For the light particles the PKA's (ion in) become important at grazing incidence as one would expect. Also the number of SKA's (ion in) is increased with increasing angle of incidence until the maximum yield is reached, but beyond this point their contribution decreases again. The contribution of the PKA's (in out) is decreasing with angle of incidence. For the heavier ions the SKA's (ion in) always remain the most important part despite their decrease with increasing angle of incidence.

Summarizing the results of this section, we may state the following: For light ions 3 processes (SKA of incident ions, SKA and PKA of reflected ions) each dominate in their respective energy range and contribute

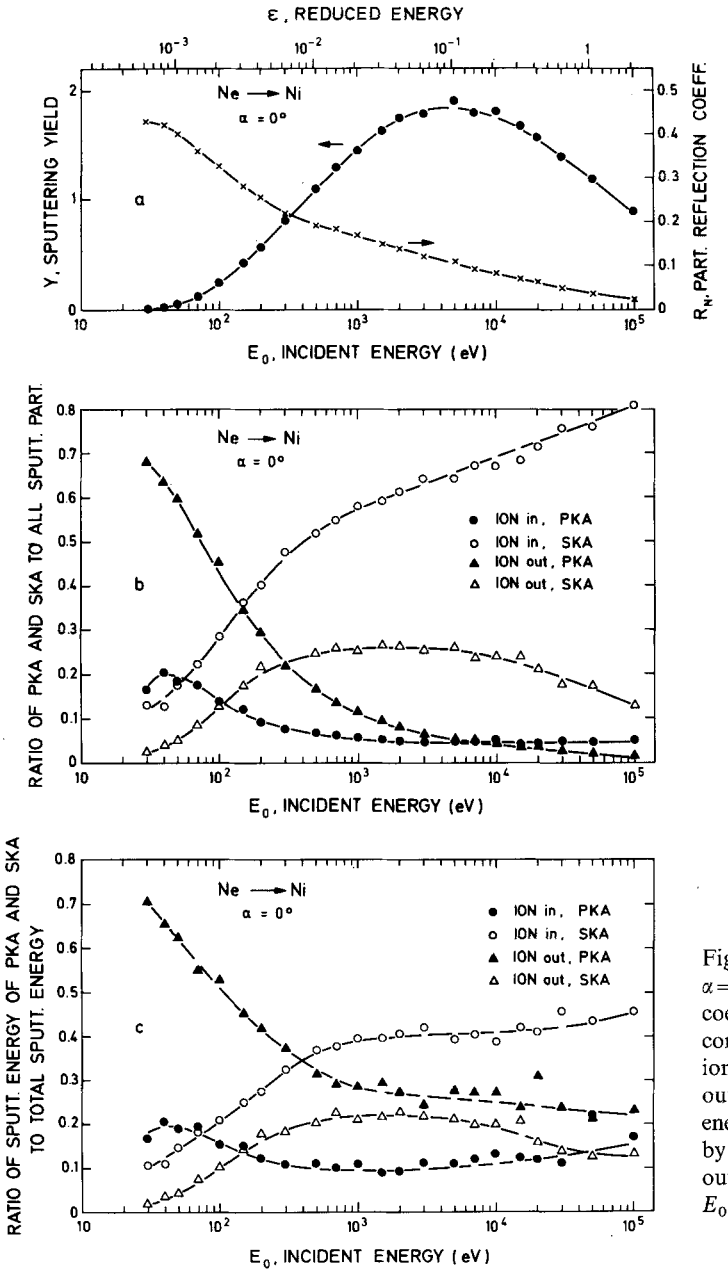

Fig. 9a–c. Ne bombardment of Ni at normal incidence, $\alpha = 0°$. (a) Sputtering yield Y and particle reflection coefficient R_N versus the incident energy E_0. (b) Relative contributions of primary knock-on atoms, PKA (ion in and ion out), and secondary knock-on atoms (ion in and ion out), to the total sputtering yield Y versus the incident energy E_0. (c) Relative contributions of the energy carried by PKA's (ion in and ion out) and SKA's (ion in and ion out) to the total sputtered energy versus the incident energy E_0. Lines drawn to guide the eye

in the keV-range in about equal parts to sputtering. For heavy ions of energies above 2 keV the SKA's of the incident ions dominate the sputtering effect, and hence the model of collision cascades should apply well. Littmark's and Fedder's model [9] should be applicable for light ions below 0.2 keV according to the present findings.

2.3. Dependence of the Sputtering Yield on the Surface Binding Energy

In the transport theory [8] the sputtering yield is inversely proportional to the surface binding energy E_S. This is checked for Ne bombardment of Ni at normal incidence in Fig. 16. Three incident energies are chosen: one near the threshold, one left of the maximum and another at an energy above the maximum yield. At low energies the dependence of the yield on the surface binding energy is much stronger whereas at the highest energies investigated the dependence is weaker than the inverse proportionality.

2.4. Sputtering Yield as a Function of Ion Energy

In Fig. 17 the sputtering yield versus the incident energy E_0 is given for H, D, He, Ne, Ar, and Xe bombardment of Ni. An energy range of nearly four

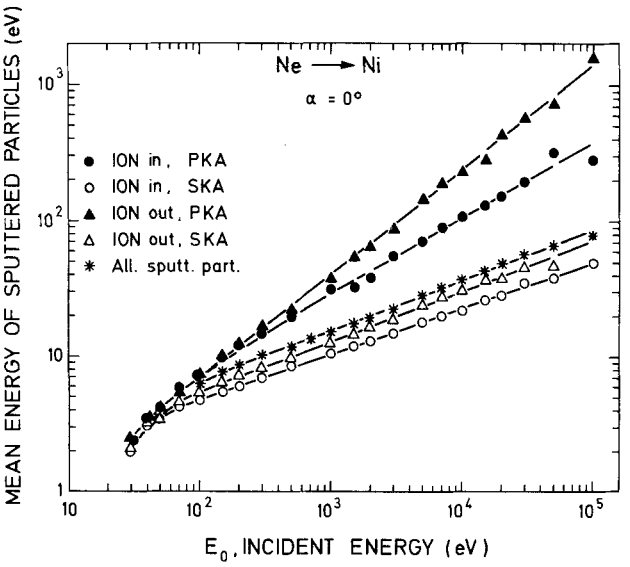

Fig. 10. Ne bombardment of Ni at normal incidence, $\alpha = 0$. Mean energy of PKA's (ion in and ion out), SKA's (ion in and ion out) and of all sputtered particles versus the incident energy E_0. Lines drawn to guide the eye

orders of magnitude (30 eV to 200 keV) was covered. For comparison experimental data for the light ions [25, 46, 47] and heavy ions [Ref. 3, Chap. 4, 24, 25, 46, 48–53] are included in the figure. The overall agreement between our prediction and the experimental data is excellent if one remembers that no adjustment has been made. The surface binding energy, $E_S = 4.46$ eV, for Ni was taken from a table [26]. Another comparison with experimental data for Mo bombarded with H, D, and ^{4}He is shown in [20].

2.5. *Sputtering Yield as a Function of the Angle of Incidence*

The dependence of the sputtering yield on the angle of incidence is shown in Fig. 18 for H on Ni. It can be seen that at low energies there exists only a weak maximum of the sputtering yield vs. angle. It develops above 200 eV incident energy and shifts to larger angles of incidence with increasing energy. The ratio of the maximum value to the yield at normal incidence increases with incident energy. The agreement with experimental data is reasonably good. It seems that at angles $\alpha < 50°$ the calculated values are somewhat too low, but the reproducibility of experimental values is sometimes not better than 50%. There is always the question of the influence of surface roughness. Other comparisons of TRIM results with experimental data for Fe, Ni, Mo, Au bombarded with H, D, T, ^{4}He are given in [16, 17, 20].

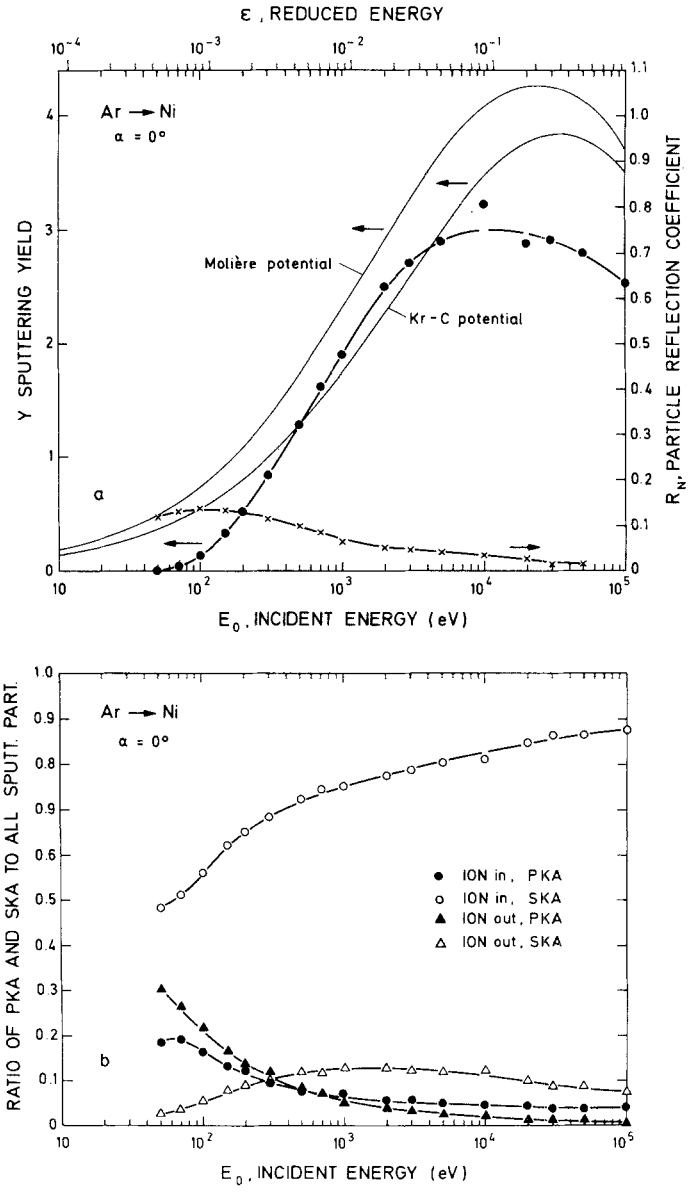

Fig. 11a and b. Ar bombardment of Ni at normal incidence, $\alpha = 0°$. (a) Sputtering yield Y and particle reflection coefficient R_N versus incident energy E_0. In addition, the sputtering yield is shown as calculated from Sigmund's theory, using $F_D(x=0) = \alpha \cdot S_n(E_0)$ for both the Molière and the Kr–C potential. (b) Relative contributions of primary knock-ons, PKA (ion in and ion out), and secondary knock-ons, SKA (ion in and ion out) to the total sputtering yield Y versus incident energy E_0. Lines drawn to guide the eye

2.6. *Angular Distributions of Sputtered Particles*

For normal incidence the angular distributions are usually expected to be not far from cosine [Ref. 3, Chap. 2, 13, 15]. This is checked for Ne-bombardment of Ni at several incident energies and at a fixed energy for several different incident projectiles.

Figure 19 shows the angular distributions of sputtered particles in a graph for easy comparison with a cosine

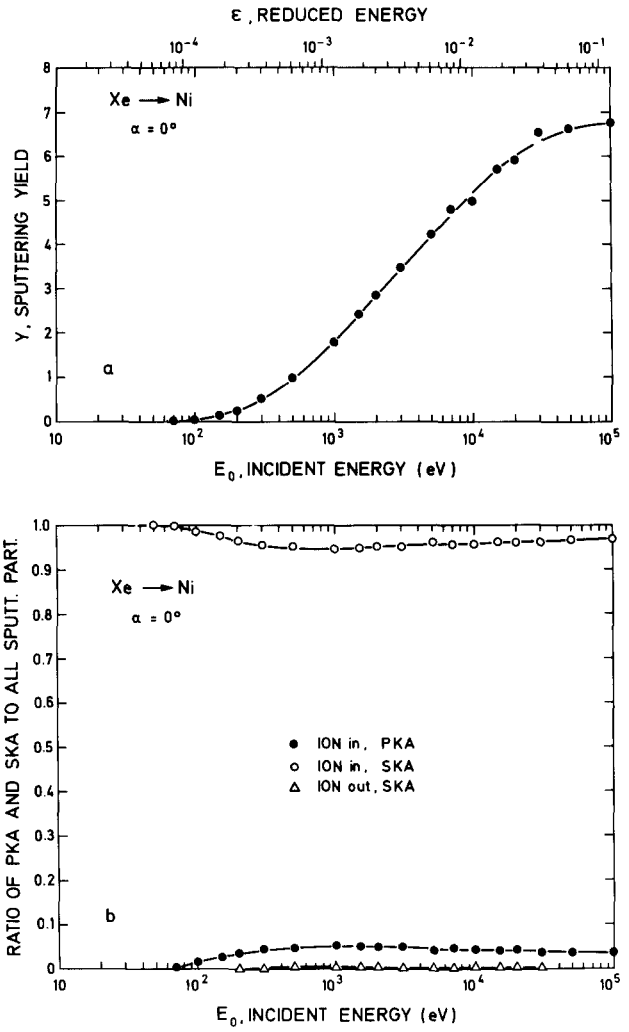

Fig. 12a and b. Xe bombardment of Ni at normal incidence, $\alpha = 0°$. (a) Sputtering yield Y versus the incident energy E_0. (b) Relative contributions of primary knock-ons, PKA (ion in and ion out), and secondary knock-ons, SKA (ion in and ion out) to the total sputtering yield Y versus incident energy E_0. Lines drawn to guide the eye

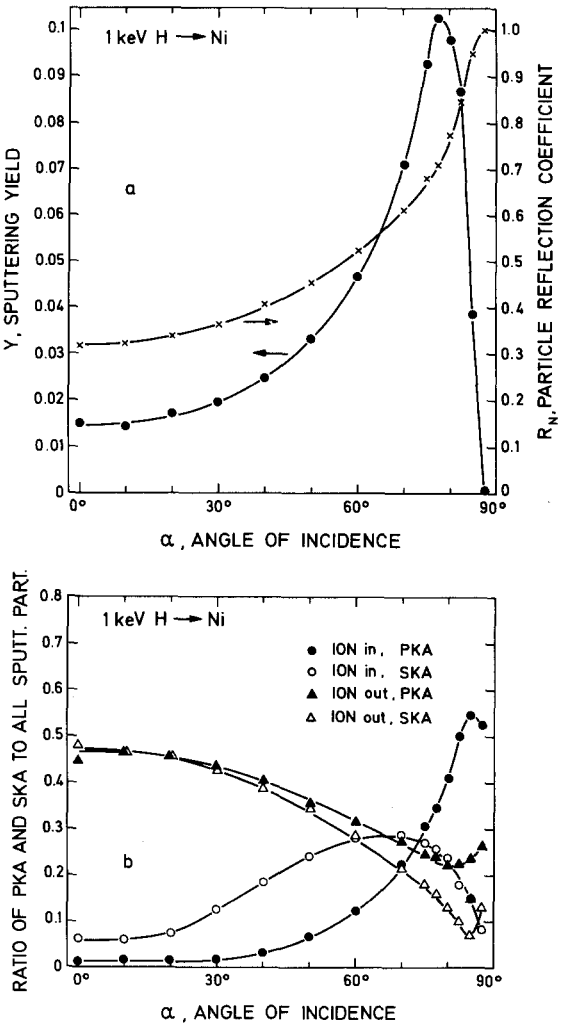

Fig. 13a and b. H bombardment of Ni at an incident energy $E_0 = 1$ keV: (a) Sputtering yield Y and particle reflection coefficient R_N versus the angle of incidence α. (b) Relative contributions of primary knock-ons, PKA (ion in and ion out), and secondary knock-ons, SKA (ion in and ion out), to the total sputtering yield Y versus the angle of incidence α. Lines drawn to guide the eye

distribution (straight line). At low projectile energy the distribution is undercosine (less sputtered particles in a direction normal to the target surface), at incident energies around 200–300 eV it is about cosine, and the distribution is overcosine for higher energies with no change in the distributions between 5 and 100 keV. This applied for Ne bombardment of Ni. For several incident projectiles the angular distributions at 1 keV are similar and somewhat overcosine. The figure also shows that for a bulk binding energy $E_B = E_S$ the angular distribution is the same as for $E_B = 0$ eV. Newer experimental results [54, 55] seem to confirme the trend in TRIM.SP results exhibiting a slight overcosine distribution for not too low energies.

For non-normal incidence the azimuthal symmetry, which is valid for normal incidence (and an amorphous target), is gone. This fact is clearly demonstrated in Fig. 20, where the azimuthal distribution (integrated over the polar angle) of the sputtered particles is shown for Ni bombarded with 1 keV H at an angle of incidence $\alpha = 80°$. The highest intensity does not change from the forward direction ($\varphi = 0$) to about $\varphi = \pm 30°$, giving the distribution a butterfly-like shape. The PKA's make an appreciable contribution.

Because of the azimuthal asymmetry it is not reasonable to show total polar angle distributions (integrated over the azimuthal angle) of sputtered particles. The polar angle distribution has been investigated ex-

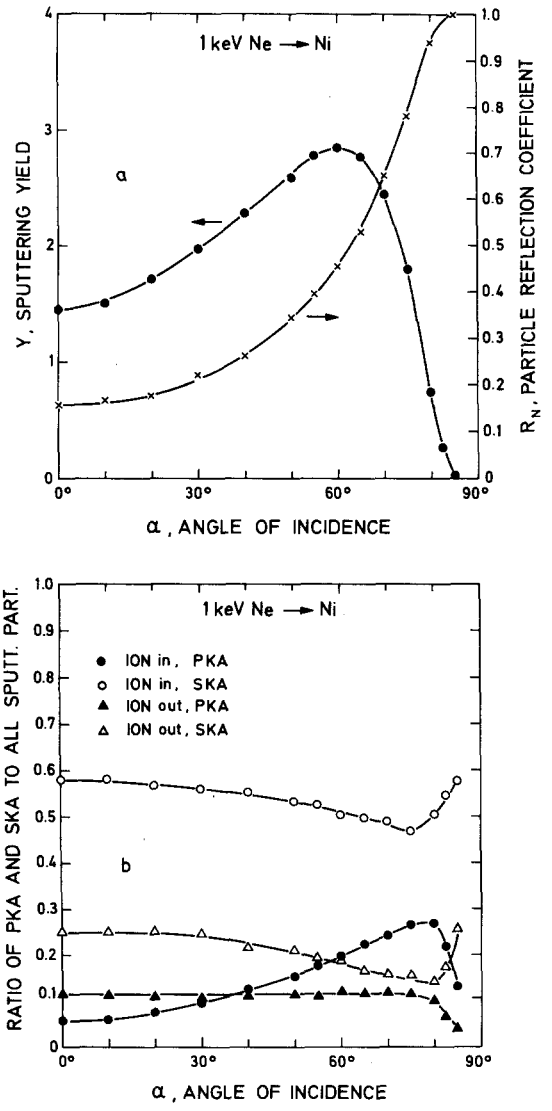

Fig. 14a and b. Ne bombardment of Ni at an incident energy $E_0 = 1$ keV: Description the same as for Fig. 13

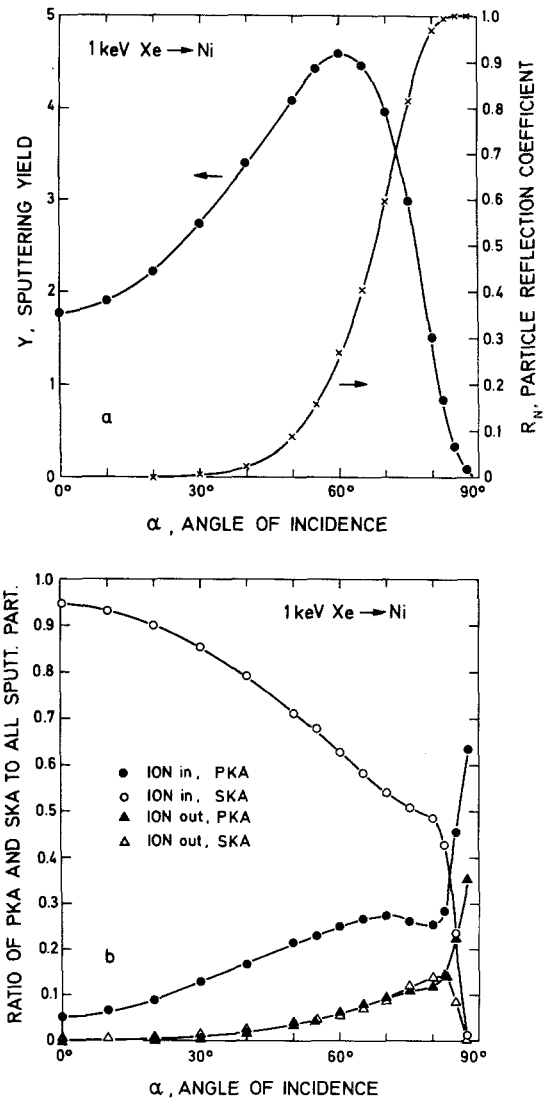

Fig. 15a and b. Xe bombardment of Ni at an incident energy $E_0 = 1$ keV: Description the same as for Fig. 13

perimentally for the incident plane ($\varphi = 0$) [15]. Figure 21 gives calculated polar angle distributions in the incident plane, where the intensity has been integrated over an azimuthal angle between 0° and 15°. The dependence on the angle of incidence at a fixed incident energy, as shown in Fig. 21a, demonstrates that the maximum of the distribution is moving from about $\beta = 40°$ at $\alpha = 85°$ to $\beta = 55°$ at $\alpha = 75°$ and for an even larger incident angle $\alpha = 70°$ the distribution is much broader with a less pronounced maximum at $\beta = 33°$. The dependence on the incident energy at a fixed incident angle, shown in Fig. 21b, is even stronger than for the incident angle, The maximum of the distribution at 0.40 keV is at $\beta = 62°$ moving to somewhat less than $\beta = 30°$ at energies above 4 keV. For higher energies the dependence is much weaker. Figure 21c gives an example how these angular distributions change for different ion target combinations for the same incident energy and angle. A comparison with experimental distributions is not performed, because the angular resolution in the experiments was not sufficient. Nevertheless the experimental data show some similarity with those shown in Fig. 21. Distributions calculated with an analytical theory [56] are usually broader than the distributions determined by TRIM [15].

A complete angular distribution of sputtered particles is shown in Fig. 22a for Ni bombarded with 4 keV D at $\alpha = 80°$. The form chosen here is a contour plot, where lines of equal intensity in a fixed solid angle are plotted versus the polar and azimuthal angle. The intensity step between adjacent contour lines is given by c in

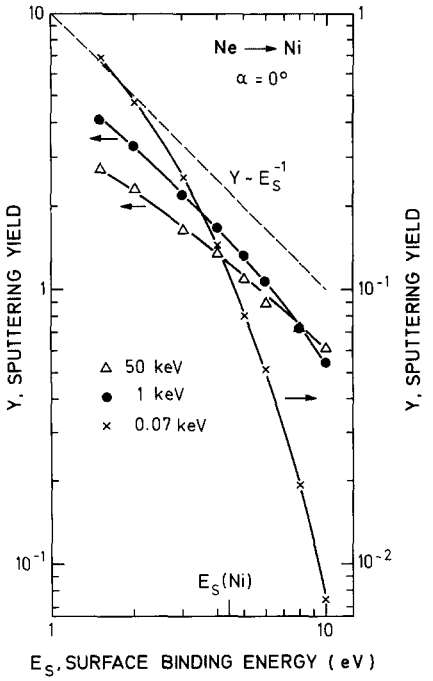

Fig. 16. Ne bombardment of Ni at normal incidence, $\alpha = 0°$, and for three incident energies, $E_0 = 0.07$, 1.0, and 50 keV. The sputtering yield Y is plotted versus the surface binding energy E_S. The dashed line gives $Y \propto E_S^{-1}$ [8]

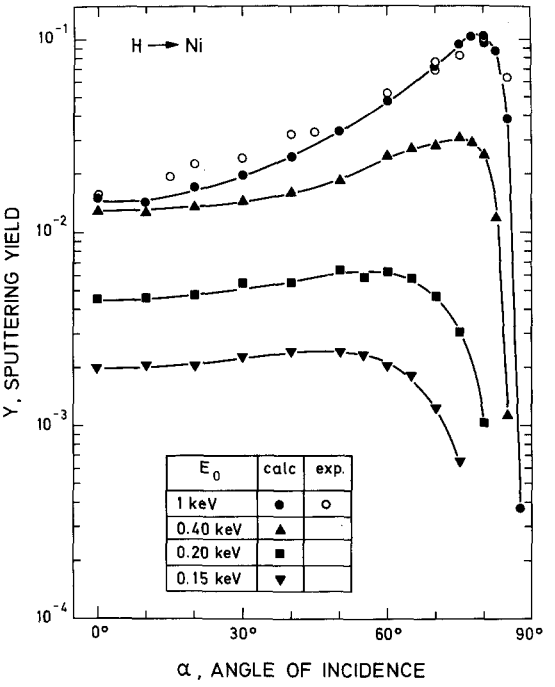

Fig. 18. Comparison of experimental [47] and calculated values of the sputtering yield Y versus the angle of incidence α for H on Ni. Incident energies, $E_0 = 0.15$, 0.2, 0.4, and 1.0 keV. Lines connect the calculated points and are drawn to guide the eye

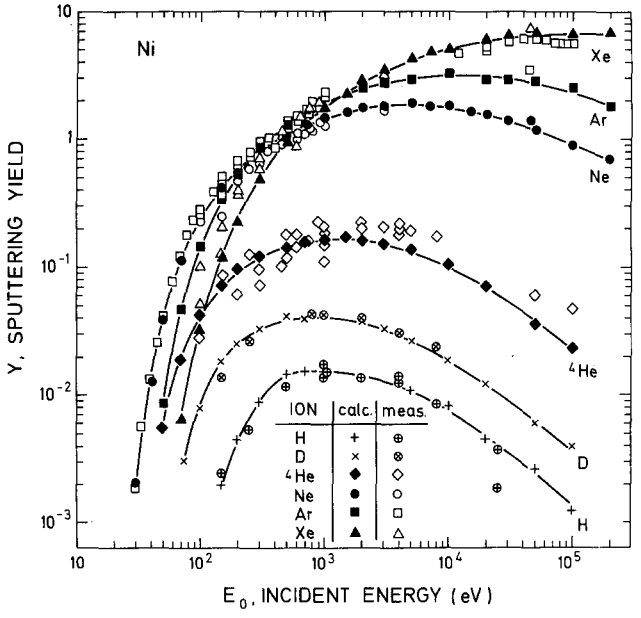

Fig. 17. Comparison of experimental [Ref. 3, Chap. 4] and [24, 25, 46–53] and calculated values of the sputtering yield Y versus incident energy E_0 for H, D, ^{4}He, Ne, Ar, and Xe on Ni at normal incidence. Lines connect the calculated points and are drawn to guide the eye

arbitrary units. For normal incidence a cosine distribution would give lines parallel to the azimuthal axis with a maximum intensity for a polar angle $\beta = 45°$. But for the example picked in Fig. 22a a ridge of high intensity starting at ($\varphi = 0$, $\beta \sim 24°$) extends up to ($\varphi = 70°$, $\beta = 90°$). The existence of such a ridge has been verified experimentally [39]. This experimental distribution, shown in Fig. 22b, clearly shows the ridge at the same angular positions but it is not as well defined as in the calculated distribution because of the limited experimental angular resolution.

The existence of the ridge is a consequence of the large contribution of PKA to the sputtering yield. This is demonstrated in Fig. 22c and d. Figure 22c shows the complete angular distribution created only by PKA, whereas Fig. 22d gives the distribution for the SKA only. The SKA are nearly homogeneously distributed and show no indication of a ridge. This ridge is only created by PKA. The sum of both distributions in Fig. 22c and d gives the distribution in 22a.

Polar angle distributions as shown in Fig. 21 are a cut through the contour plot in Fig. 22a at $\varphi = 0$. The maximum in the distributions in Fig. 21 give the starting point of the ridge. As long as a pronounced maximum in Fig. 21 exists there will be always a pronounced ridge in the contour plot of the complete angular distribution. As the starting point of the ridge

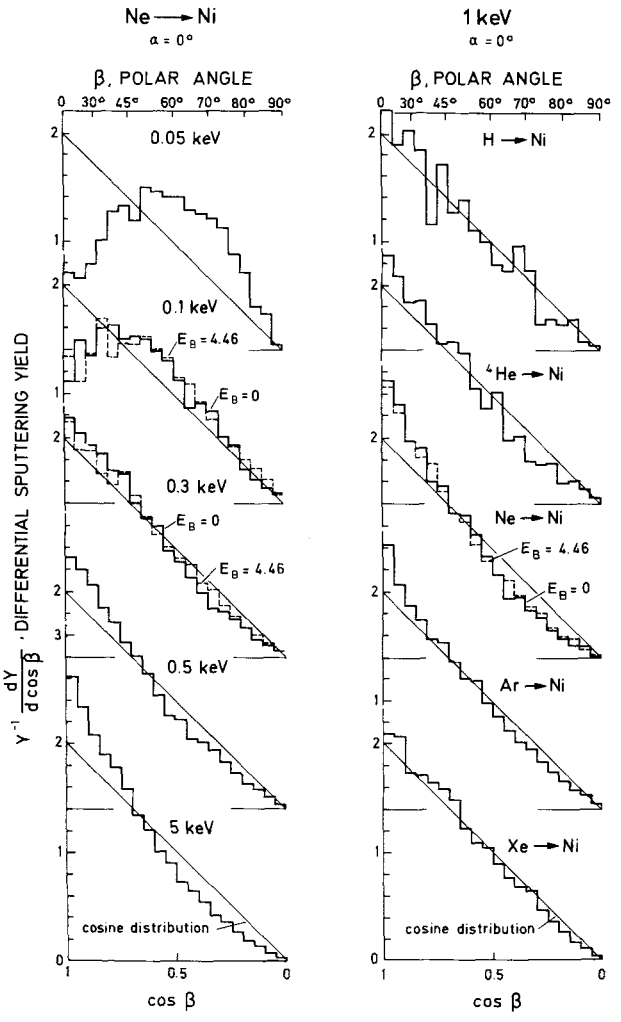

Fig. 19a and b. The differential sputtering yield versus the cosine of the polar emission angle β of the sputtered particles for normal incidence, $\alpha = 0$. The straight line indicates a cosine distribution. The dashed distribution is calculated with $E_B = E_S = 4.46$ eV. (a) Ne bombardment of Ni, 5 incident energies E_0. (b) Bombardment of Ni with several incident ions at an incident energy, $E_0 = 1$ keV

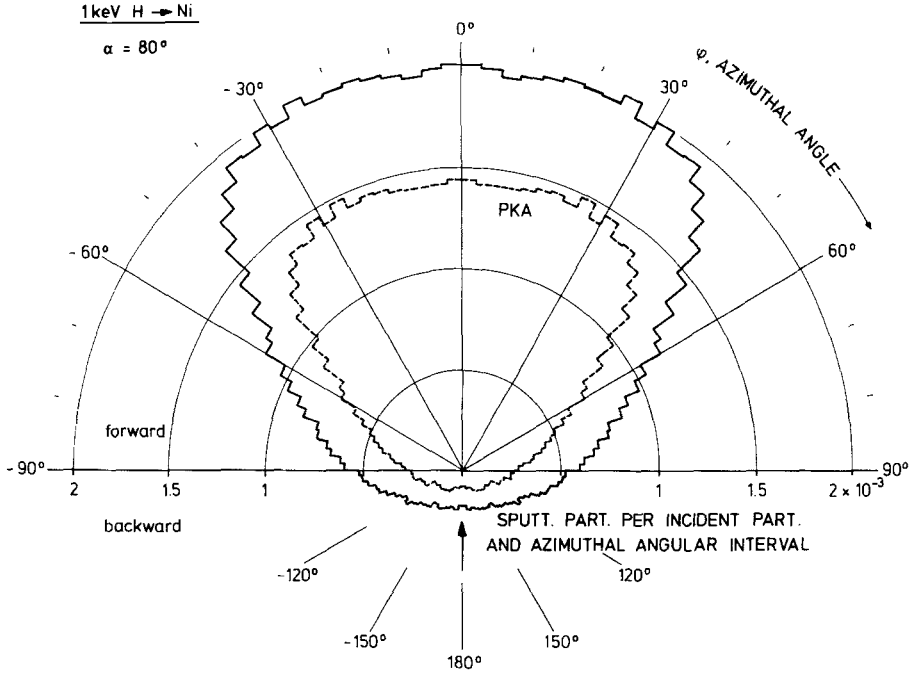

Fig. 20. Azimuthal distribution (integrated over polar angles) of sputtered particles for 1 keV H bombardment of Ni at an angle of incidence, $\alpha = 80°$

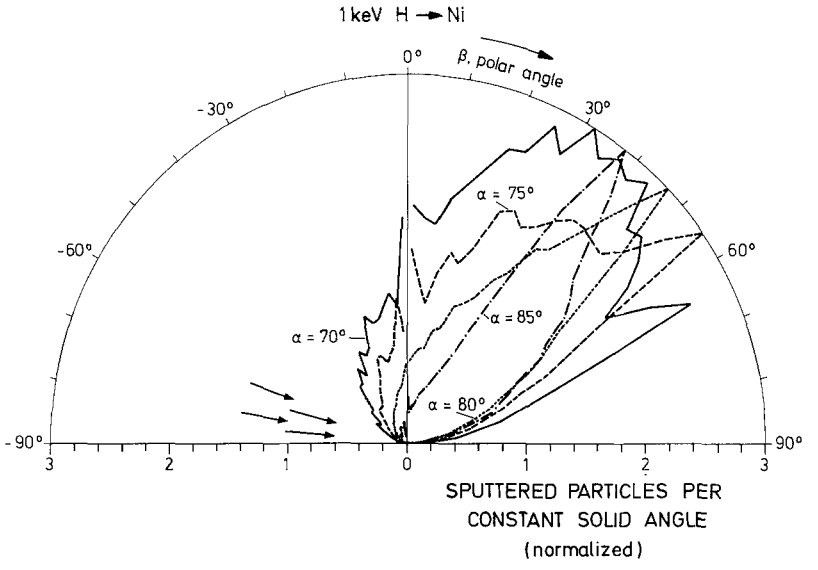

Fig. 21a

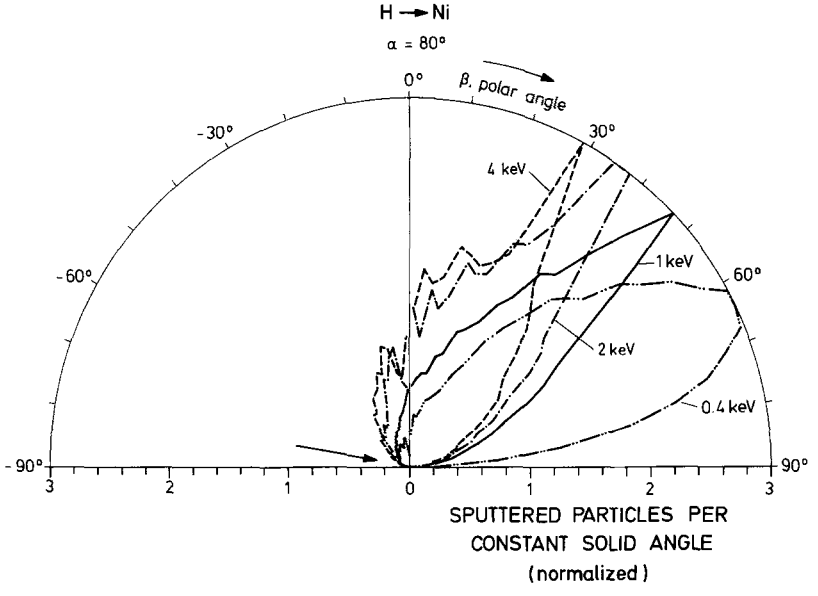

Fig. 21b

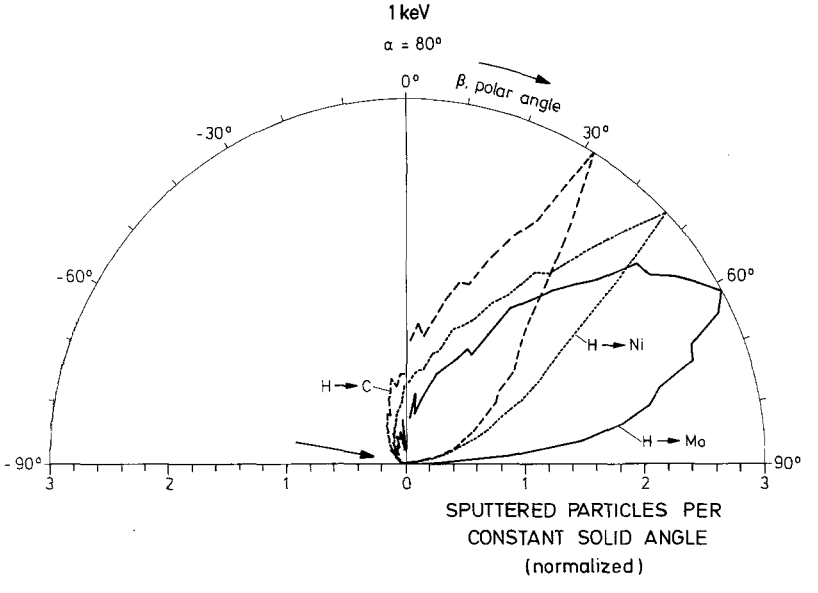

Fig. 21. (a) Angular distributions in the incident plane of the sputtered particles (azimuthal angular range $0° \leqq \varphi < 15°$) for 1 keV H bombardment of Ni at several angles of incidence. The distributions are normalized to give the same maximum value. (b) Angular distributions of sputtered particles in the incident plane (azimuthal angular range $0° \leqq \varphi < 15°$) for H bombardment of Ni at an angle of incidence, $\alpha = 80°$, and for several incident energies E_0. The distributions are normalized to give the same maximum value. (c) Angular distributions of sputtered particles in the incident plane (azimuthal angular range $0° \leqq \varphi < 15°$) for three ion-target combinations at an incident angle, $\alpha = 80°$. The distributions are normalized to give the same maximum value

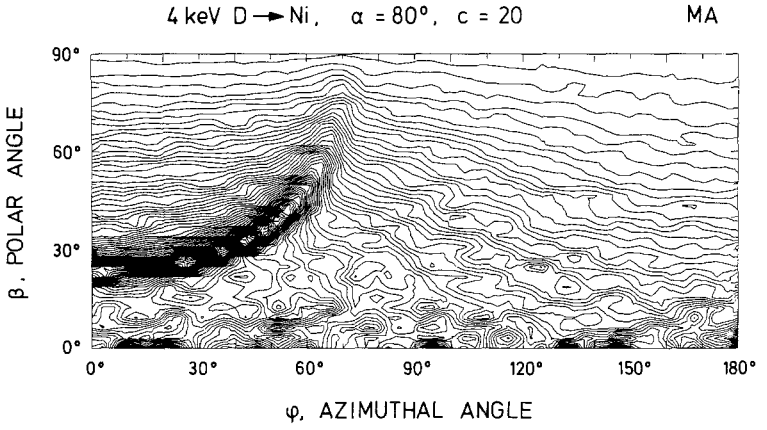

Fig. 22a

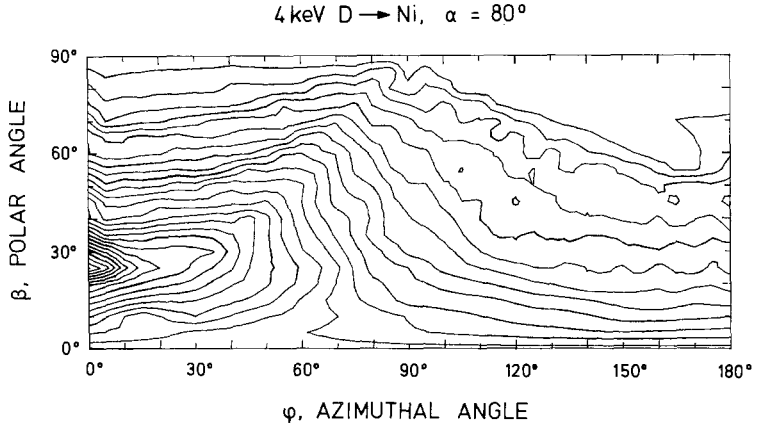

Fig. 22b

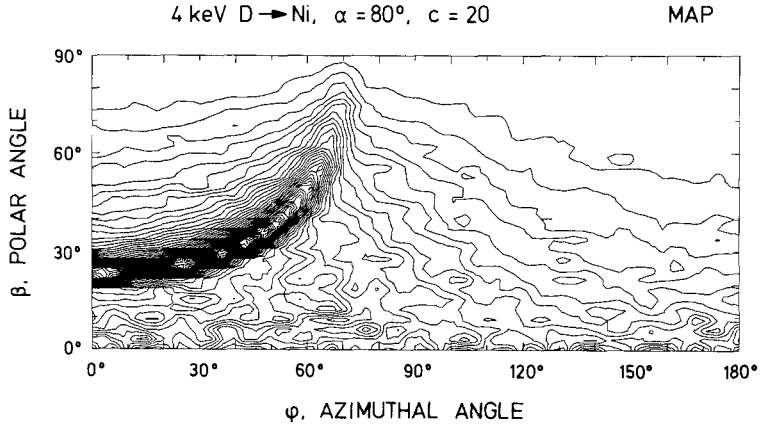

Fig. 22c

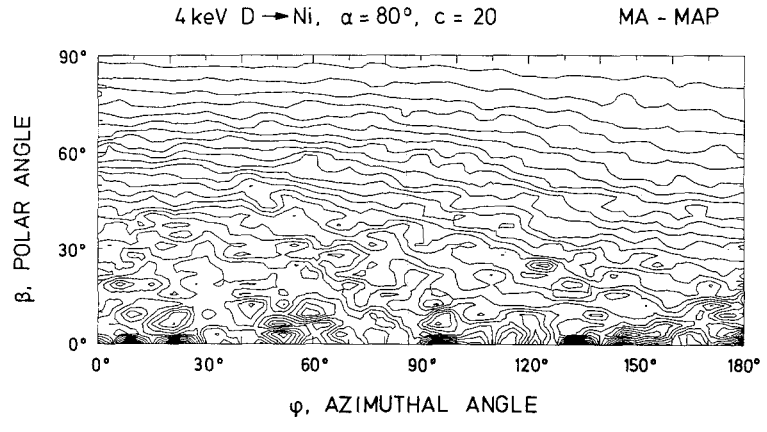

Fig. 22a–d. Contour plots (lines of equal intensity: sputtered atoms per solid angle) of the angular distribution of sputtered particles for D bombardment of Ni at an incident energy of 4 keV and an angle of incidence of $\alpha = 80°$. (a) Angular distribution of all sputtered particles; (b) experimentally determined angular distribution [39]; (c) angular distribution of primary knock-ons (PKA); (d) angular distribution of secondary knock-ons (SKA)

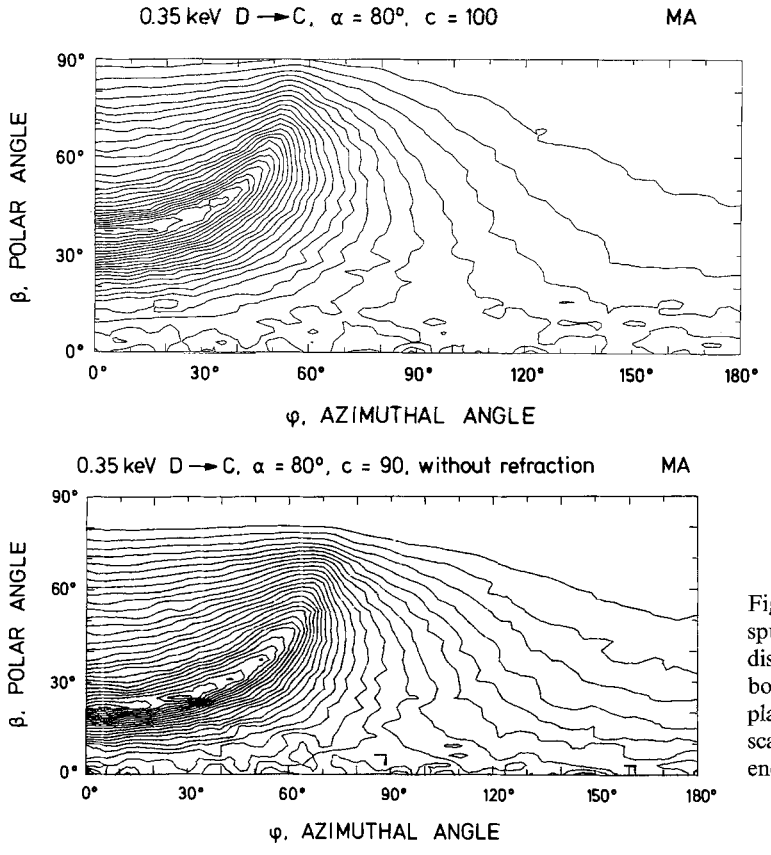

Fig. 23a

Fig. 23a and b. Contour plots (lines of equal intensity: sputtered atoms per solid angle) of the angular distribution of sputtered particles for 350 eV D bombardment of C at an incident angle, $\alpha = 80°$. (a) planar potential, surface binding energy, $E_S = 7.4$ eV. (b) scalar potential (without refraction), surface binding energy, $E_S = 7.4$ eV

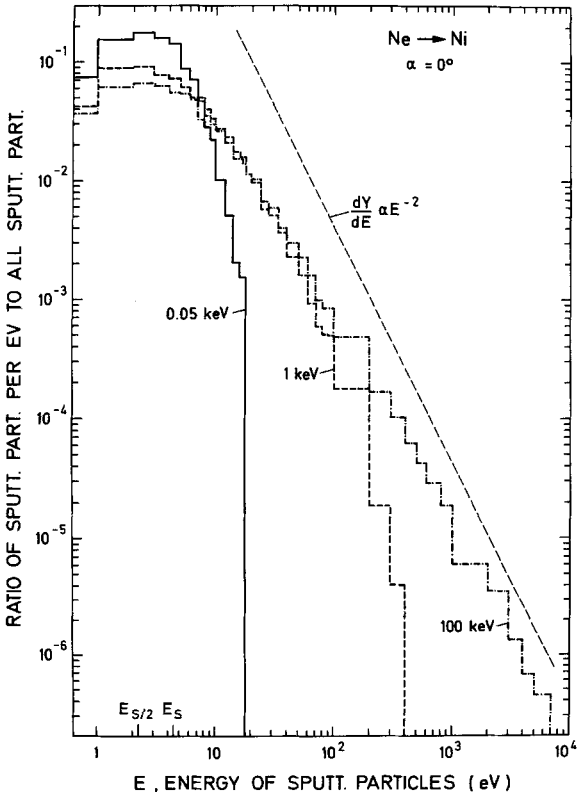

Fig. 24. Energy distributions of sputtered particles for Ne bombardment of Ni for three incident energies E_0 and normal incidence, $\alpha = 0$. The dashed line indicates a E^{-2} distribution

(at $\varphi = 0$) moves up to larger polar angles β with increasing incident energy or decreasing incident angle, the ridge becomes less pronounced and more compressed in the azimuthal angle φ. If the distribution in the incident plane becomes broader as for example the distribution for $\alpha = 70°$ in Fig. 21a, the ridge in the correspondent contour plot disappears. For heavier ions, as for example Ni bombarded with 1 keV Ar at $\alpha = 60°$, the ridge is only weakly developed. More examples are shown in [57]. The formation and the position of the ridge can be understood by sputtering due to binary collisions [58, 57]. The possibility of sputtering by binary collisions at glancing angle conditions was first pointed out by Henschke [59].

In Fig. 23a and b a comparison is made of the complete angular distributions calculated with a planar potential and with a scalar potential (without refraction). The example chosen is *C* bombarded with 350 eV *D* at $\alpha = 80°$. Both distributions look somewhat similar but there are differences: The ridge starts at nearly $\beta = 40°$ for the planar potential whereas the starting point of the ridge for the scalar potential is at about $\beta = 25°$. An experiment should easily distinguish between both surface potential models. Other differences are that the ridge is more compressed in φ for the planar potential and that there is less intensity for large polar angles in the case of the scalar potential. The density of the

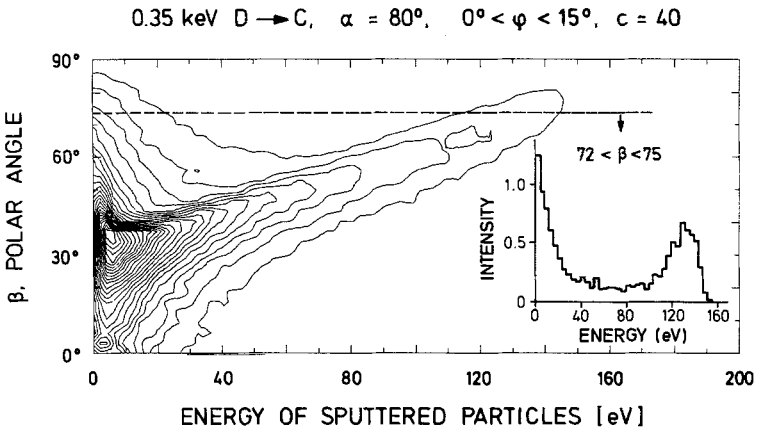

Fig. 25a

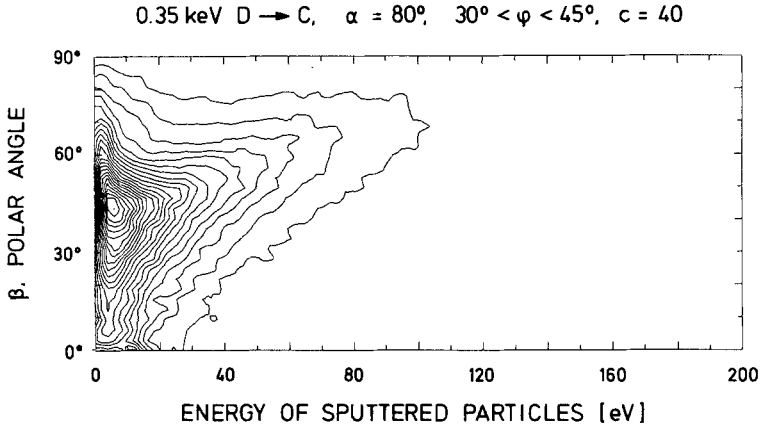

Fig. 25b

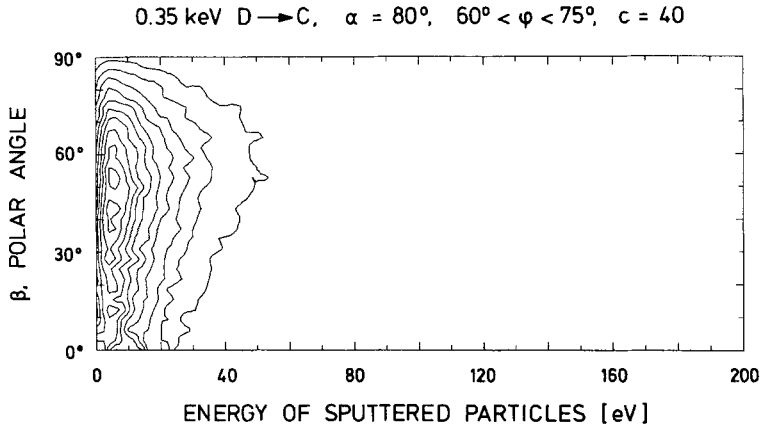

Fig. 25a–c. Contour plot (lines of equal intensity: sputtered atoms per solid angle) of the energy-polar angle distribution of sputtered particles in three azimuthal angular regions, $\Delta\varphi$, for 350 eV bombardment of C with D at an angle of incidence, $\alpha = 80°$. (a) $0 \leqq \varphi < 15°$, the insert gives the energy distribution in the polar angular region $72° \leqq \beta < 75°$. (b) $30° \leqq \varphi < 45°$. (c) $60° \leqq \varphi < 75°$

contour lines also shows that the sputtering yield for the scalar potential is higher than for the planar potential [8]. Both calculations were performed with the same number of incident particles.

2.7. *Energy Distributions of Sputtered Particles*

Energy distributions of Ni atoms sputtered by Ne at three incident energies are shown in Fig. 24. All three energy distributions exhibit a maximum at about half the surface binding energy in agreement with an earlier prediction by Thompson [60]. For the highest incident energy the distribution decreases proportional to E^{-n} *with* $n \simeq 5/3$ over three orders of magnitude in the energy of the sputtered particles. This value of n is somewhat smaller than the value $n = 2$ in [60]. Comparing the analytical formula in [Ref. 3, Chap. 2] and [8] with the calculated distribution in Fig. 24 gives a value $m = 1/6$ for the exponent in the power potentials used in [Ref. 3, Chap. 2] and [8] and shifts the maximum of the distribution to $0.6\,E_S$. The value $m = 1/6$ also

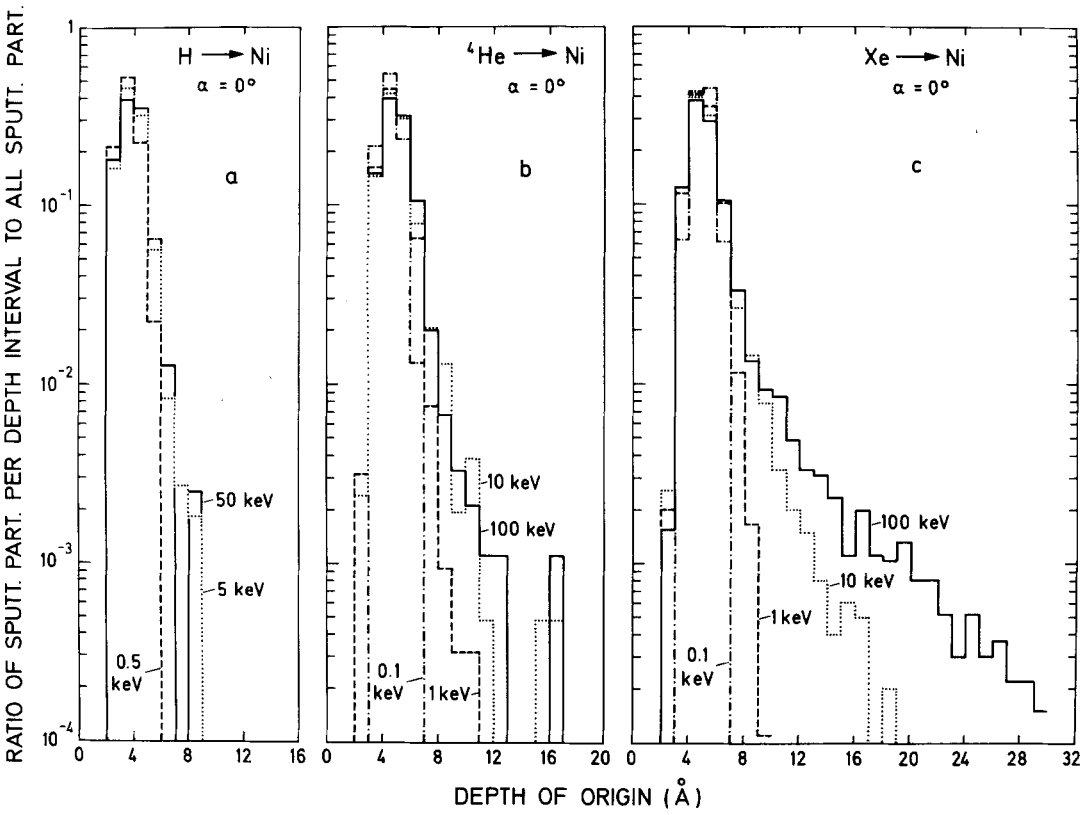

Fig. 26a–c. Relative number of sputtered particles versus their depth of origin for bombardment of Ni at normal incidence (there are no target atoms for $0 < x < 2\,P_{max} = 2.56$ Å). (a) H bombardment, incident energies $E_0 = 0.5$, 5, and 50 keV. (b) ^{4}He bombardment, incident energies $E_0 = 0.1$, 1, 10, and 100 keV. (c) Xe bombardment, incident energies $E_0 = 0.1$, 1, 10, and 100 keV

implies a sputtering yield Y proportional to $E_S^{-2/3}$ in the analytical theory which is in good agreement with the dependence for the high incident energy bombardment in Fig. 16. At intermediate incident energies the slope is about the same until the distributions come close to the maximum transferrable energy in a binary collision. For incident energies near the threshold the distributions fall off much steeper due to the low cut-off energy. – Energy distributions of sputtered particles calculated earlier with TRIM.SP have already compared to theoretical and experimental distributions in [13, 15]. – It should be mentioned here that the above discussed total energy distributions need not coincide with energy distributions at a specific polar angle β.

For non-normal incidence the energy spectra of sputtered particles depend on the polar angle β as well as on the azimuthal angle φ. One example is shown in Fig. 25 for C bombarded with 0.35 keV D at $\alpha = 80°$. Here again a contour plot shows lines of equal intensity in a fixed solid angle versus the polar angle β and the energy of the sputtered particles for three azimuthal intervals. Energy distributions at a specific polar angle β are horizontal cuts parallel to the energy axes. In the forward direction ($0° \leqq \varphi < 15°$) energy distributions for polar angles, $\beta > 40°$, show a second maximum at higher energies as indicated by the insert in Fig. 25a. The maximum at low energies (in the eV range) is more pronounced at small polar angles β than at large β. In the azimuthal angular range $30° \leqq \varphi < 45°$ the second maximum in the energy distribution is nearly gone as seen in Fig. 25b. A further increase in the azimuthal angle reduces the intensity and gives the typical energy distributions with a maximum at some eV for all polar angles β (Fig. 25c). First experimental evidence for a high energy peak in the energy distribution of sputtered particles is found in [61] and more clearly recently in [63]. This high energy peak for grazing incidence can easily be understood partly by sputtering in binary collisions [57, 63]. In the total energy distribution as summed over the half space, no second maximum can be detected.

Results calculated with a scalar potential for the same example as in Fig. 25 show no maximum in the eV range but otherwise a similar contour plot as in Fig. 25 with the main difference that all contour lines are shifted to smaller polar angles β. Many calculated results mentioned here are shown in a more exhaustive compilation [57].

2.8. Escape Depth of Sputtered Particles

The depth of origin of the sputtered particles is usually very small [8]. Most sputtered particles are kicked out of the target from the first two layers, nearly independent of energy or angle of incidence (Fig. 26) where the examples chosen were Ni bombarded with H, ^{4}He, and Xe. Larger depths can contribute depending on the energy and kind of the incident particle. The particles from larger depths are always an insignificant fraction of all sputtered particles. This means that the depth of origin of sputtered particles is nearly independent on the incident energy, in agreement with earlier results [8, 62].

3. Summary and Concluding Remarks

This paper has shown that the Monte Carlo program TRIM.SP is well suited to reproduce experimental sputtering data, not only total yields, but also, more detailed information on angular and energy distributions of sputtered particles. Furthermore, the relative contributions of the different processes (PKA, SKA from in- or outward moving ion) to sputtering have been determined. This provides guidance for determining which one of the analytical theories is applicable. Some discrepancies with standard cascade theories were observed. The use of different inter-atomic potentials was found to influence the sputtering yields in the expected way. The choice of the inelastic energy loss model way also shown to affect the total sputtering. The effect of the surface binding energy on the sputtering yield has been investigated with the result that the yield is not exactly inversely proportional to the surface binding energy. Finally, predictions have been made of the energy and angular distributions for non-normal incidence of light ions, which could, in part, be verified by experimental findings [39, 40].

The interesting features of the sputtering of two component targets will be dealt with in a separate, forthcoming paper.

Acknowledgements. One of the authors (W.E.) would like to thank Ms. Walter for writing some of the output programs, and Ms. Hirschinger, Ms. Sombach, and Ms. Fritsch for preparing the drawings. W.E. is indebted to J. Bohdansky, J. Roth, M. T. Robinson, and P. Sigmund for many valuable discussions. We thank R. Behrisch, J. Bohdansky, W. Möller, and J. P. Schneider for critical reading of the manuscript. J. P. Biersack thanks for the hospitality of the Max-Planck-Institut for Plasmaphysik.

References

1. *Secondary Ion Mass Spectrometry* SIMS II–IV, ed. by A. Benninghoven et al., Springer Ser. Chem. Phys. **9**, **19**, **36** (Springer, Berlin, Heidelberg, New York 1979, 1982, 1984)
2. Data Compendium for Plasma-Surface Interactions by R. A. Langley, J. Bohdansky, W. Eckstein, P. Mioduszewski, J. Roth, E. Taylauer, E. W. Thomas, K. L. Wilson, H. Verbeek: Nucl. Fusion (1984, in press)
3. R. Behrisch (ed.): *Sputtering by Ion Bombardment* I, Topics Appl. Phys. **47** (Springer, Berlin, Heidelberg, New York 1981)
4. D.P. Jackson: In Proc. of the Symp. Sputtering, ed. by Varga, Betz, Viehböck, Inst. f. Allgem. Physik, TU Wien (1980)
5. D.E. Harrison: Radiat. Eff. **70**, 1 (1983)
6. J. Lindhard, V. Nielsen, M. Scharff: Mat. Fys. Medd. Dan. Vid. Selsk. **36**, 10 (1968)
7. K.B. Winterbon, P. Sigmund, J.B. Sanders: Mat. Fys. Medd. Dan. Vid. Selsk. **37**, 14 (1970)
8. P. Sigmund: Phys. Rev. **184**, 383 (1969) and **187**, 768 (1969)
9. U. Littmark, S. Fedder: Nucl. Instrum. Methods **194**, 607 (1982)
10. J.P. Biersack, L.G. Haggmark: Nucl. Instrum. Methods **174**, 257 (1980)
11. K.H. Ecker, J.P. Biersack: 7th Intern. Conf. on Atomic Collisions in Solids, Moscow (1977)
    K.H. Ecker, K.L. Merkle: Phys. Rev. B **18**, 1020 (1978)
12. L.G. Haggmark, W.D. Wilson: J. Nucl. Mater. **76/77**, 149 (1978)
13. J. Bohdansky: J. Nucl. Mater. **93/94**, 44 (1980)
14. J.P. Biersack: "Sputtering Predictions by the Monte Carlo Program TRIM.SP", Proc. of the Symposium on Sputtering, ed. by P. Varga, G. Betz, R.P. Viehböck, Techn. Universität Wien (1980) p. 112
15. J. Roth: In Proc. of the Symposium on Sputtering, ed. by Varga, Betz, Viehböck, Techn. Univers. Wien (1980) p. 773
16. L.G. Haggmark, J.P. Biersack: J. Nucl. Mater. **93/94**, 664 (1980)
17. L.G. Haggmark, J.P. Biersack: J. Nucl. Mater. **103/104**, 345 (1981)
18. J. Bohdansky, G.L. Chen, W. Eckstein, J. Roth: J. Nucl. Mater. **103/104**, 339 (1981)
19. W. Eckstein: IPP-JET-Report No. 4 (1981)
20. J. Bohdansky, G.L. Chen, W. Eckstein, J. Roth, B.M.U. Scherzer, R. Behrisch: J. Nucl. Mat. **111/112**, 717 (1982)
21. O.S. Oen, M.T. Robinson: Nucl. Instrum. Methods **132**, 647 (1976)
22. M.T. Robinson: Oak Ridge Nat. Lab., Report ORNL-4556, 1970
23. This kind of presentation was first chosen by M.T. Robinson (private communication)
24. O. Almèn, G. Bruce: Nucl. Instrum. Methods **11**, 257 (1961)
25. D. Rosenberg, D.K. Wehner: J. Appl. Phys. **33**, 1842 (1962)
26. N. Matsumami, Y. Yamamura, Y. Itikawa, N. Itoh, Y. Kazumata, S. Miyagawa, K. Morita, R. Shimizu: IPPJ-AM-14, Institute of Plasma Physics, Nagoya University, Nagoya, Japan (1980)
    R. Hultgren, J.P. Desai, D.T. Hawkins, M. Gleiser, K.K. Kelley, D.D. Wagman: Selected Values of the Thermodynamic Properties of the Elements (Am. Soc. Metals, Metals Park, Ohio, USA 1973)
27. P. Sigmund: Rev. Roum. Phys. **17**, 969 (1972) and private communication
28. M.T. Robinson: J. Appl. Phys. **54**, 2650 (1983)
29. G. Molière: Z. Naturforsch. A**2**, 133 (1947)
30. W. Wilson, L. Haggmark, J. Biersack: Phys. Rev. B **15**, 2458 (1977)
31. O.B. Firsov: Sov. Phys. JETP **6**, 534 (1958)
32. H. Oetzmann, S. Kalbitzer,: Radiat. Eff. **47**, 57 (1980)

33. P. Loftager, F. Besenbacher, O.S. Jensen, V.S. Sørensen: Phys. Rev. A **20**, 1443 (1979)
34. J.P. Biersack, J.F. Ziegler: In *Ion Implantation Techniques*, ed. by H. Rüssel and H. Glawischnig (Springer, Berlin, Heidelberg, New York 1982) p. 122
J. O'Connor, J.P. Biersack: Nucl. Instrum. Methods. (1984, to be published)
35. C. Varelas, J.P. Biersack: Nucl. Instrum. Methods **79**, 213 (1970)
36. J.P. Biersack, D. Fink: In *Atomic Collisions in Solids*, Vol. 2 (Plenum Press, New York 1975) p. 737
37. H.H. Andersen, J.F. Ziegler: Hydrogen Stopping Powers and Ranges in All Elements (Pergamon Press, New York 1977)
J.F. Ziegler: Helium Stopping Powers and Ranges in All Elements (Pergamon Press, New York 1977)
38. J. Lindhard, M. Scharff: Mat.-Fys. Medd., Dan. Vid. Selsk. **27**, 15 (1953)
39. R. Becerra-Acevedo, J. Roth, W. Eckstein, J. Bohdansky: Nucl. Instrum. Methods (1984, in press)
40. P.J. Schneider, W. Eckstein, H. Verbeek: Nucl. Instrum. Methods (1984, in press)
41. R. Weissmann, R. Behrisch: Radiat. Eff. **19**, 69 (1973)
42. R. Behrisch, G. Maderlechner, B.M.U. Scherzer, M.T. Robinson: Appl. Phys. **18**, 391 (1979)
43. T.J. Hoffman, H.L. Dodds, Jr., M.T. Robinson, D.K. Holmes: Nucl. Sci. Eng. **68**, 204 (1978)
44. M.T. Robinson: Private communication
45. W. Eckstein, H. Verbeek: IPP-Report 9/32 (1979)
46. H. Fetz, H. Oechsner: In Proc. 6 Intern. Conf. Phénoménes d'Ionisations dans les Gaz, Paris (1963) p. 39
47. J. Roth, J. Bohdansky, W. Ottenberger: IPP-Report 9/26 (1979)
48. N. Lagreid, G.K. Wehner: J. Appl. Phys. **32**, 365 (1961)
49. C.H. Weijsenfeld, A. Hoogendoorn, M. Koedam: Physica **27**, 763 (1961)
50. C. Fert, N. Colombie, B. Fagot, Pham van Chuong: In Le Bombardement Ionique (CNRS, Paris 1961) p. 67
51. R.V. Stuart, G.K. Wehner: J. Appl. Phys. **33**, 2345 (1962)
52. J.M. Poate, W.L. Brown, R. Homer, W.M. Augustymiak: Nucl. Instrum. Methods **132**, 345 (1976)
53. H.L. Bay, J. Bohdansky, E. Hechtl: Radiat. Eff. **41**, 77 (1979)
54. H.H. Andersen, V. Chernysh, B. Stenum, T. Sørensen, H.J. Whitlow: Surf. Sci. **123**, 39 (1982)
55. R.G. Allas, A.R. Knudson, J.M. Lambert, P.A. Treado, G.W. Reynolds: Nucl. Instrum. Methods **194**, 615 (1982)
56. H.E. Roosendaal, J.B. Sanders: Radiat. Eff. **52**, 137 (1980)
57. W. Eckstein: IPP-Report 9/41 (1983)
58. J. Roth, J. Bohdansky, W. Eckstein: Nucl. Instrum. Methods **218**, 751 (1983)
59. E.B. Henschke: Phys. Rev. **106**, 737 (1957) and **121**, 1286 (1961)
60. M.W. Thompson: Philos. Mag. **18**, 377 (1968)
61. S. Ahmad, B.W. Farmery, M.W. Thompson: Philos. Mag. A **44**, 1387 (1981)
I. Reid, B.W. Farmery, M.W. Thompson: Nucl. Instrum. Methods **132**, 317 (1976)
62. G. Falcone, P. Sigmund: Appl. Phys. **25**, 307 (1981)
63. P.J. Schneider, W. Eckstein, H. Verbeek: Nucl. Instrum. Methods **218**, 713 (1983)